



저작자표시-비영리-변경금지 2.0 대한민국

이용자는 아래의 조건을 따르는 경우에 한하여 자유롭게

- 이 저작물을 복제, 배포, 전송, 전시, 공연 및 방송할 수 있습니다.

다음과 같은 조건을 따라야 합니다:



저작자표시. 귀하는 원저작자를 표시하여야 합니다.



비영리. 귀하는 이 저작물을 영리 목적으로 이용할 수 없습니다.



변경금지. 귀하는 이 저작물을 개작, 변형 또는 가공할 수 없습니다.

- 귀하는, 이 저작물의 재이용이나 배포의 경우, 이 저작물에 적용된 이용허락조건을 명확하게 나타내어야 합니다.
- 저작권자로부터 별도의 허가를 받으면 이러한 조건들은 적용되지 않습니다.

저작권법에 따른 이용자의 권리는 위의 내용에 의하여 영향을 받지 않습니다.

이것은 [이용허락규약\(Legal Code\)](#)을 이해하기 쉽게 요약한 것입니다.

[Disclaimer](#)

공학석사 학위논문

Probing Point Defects in TEM

투과전자현미경을 이용한
점 결함 관측에 관한 전산모사 연구

2014년 2월

서울대학교 대학원
공과대학 재료공학부
윤 상 문

Abstract

Probing Point Defect Imaging

Sangmoon Yoon

Department of Materials Science and Engineering

College of Engineering

Seoul National University

Sub angstrom resolution of scanning transmission electron microscope (STEM) was achieved in early 2000s due to the introduction of Cs-corrected electromagnetic lens. Since then, there have been many attempts to exceed the detecting-limit of STEM such as single atomic imaging or light element imaging in the community of electron microscopy. Detection of heavy dopant atoms and the column of light elements have been succeeded with HADDF-STEM and ABF-STEM, respectively. However, these methods have limitation on detecting light dopant elements or vacancies. Therefore, it is necessary to introduce a new approach for detecting them. We think utilization of strain effect is a great solution for overcoming the limitation of existing methods. The strain field leads a different angular distribution by combination of

channeling effect and absorption effect. Even though strain field generated by light dopant atoms or vacancies is not that strong to modify the angular distribution significantly, there would be a specific angular region that can be distinguished from the original one. If we carry out the imaging only with electrons which are scattered toward that angular region, we expect that light dopant atoms and vacancies can be visualized.

Here, we have studied the feasibility of detecting light dopant atoms and vacancies with strain effects through the computer simulation. The strain field is simulated by structural relaxations with the first principle calculations and the propagation of electron waves is simulated with the multislice calculation, one of the dynamic scattering theory. A boron dopant atom, a vacancy in silicon and an oxygen vacancy in strontium titanate have been investigated in this study. We found that the column with a vacancy in silicon is shown 200% brighter than other columns if Cs-corrected probe was used and elastically scattered electrons toward 30mrad to 50mrad were utilized. We think the imaging with elastically scattered electrons is experimentally possible through the cold stage holder which suppresses thermal diffuse scatterings. Though we have not carried out the imaging simulation of the strontium titanate case yet, it is expected that detecting an oxygen vacancy in TiO column could be achieved with elastically scattered electrons toward 35mrad to 50mrad.

Detecting light dopant atoms and vacancies will not only be meaningful itself in the community of electron microscopy, but will also give a great contribution to other materials science communities. We hope this computer simulation study will give a clue for detecting light dopant atoms or vacancies.

Keywords: Point defect imaging, Electron microscopy, CBED/STEM, Strain contrast, Electron scattering, Dynamic scattering calculation

Student Number: 2012-20616

Contents

Abstracts	i
Contents	iv
List of Tables	vi
List of Figures	vii
Chapter 1 Introduction	1
1.1 Resolution Limit of Optical Microscopy	1
1.2 Resolution of STEM	6
1.2.1 Lateral Resolution of STEM	6
1.2.2 Longitudinal Resolution of STEM	12
1.3 Previous Attempts at Point-defect Imaging	14
1.4 New Approach for Point-defect Imaging	19
Chapter 2 Theoretical Background	21
2.1 Scattering Theory	21
2.1.1 Kinematic Scattering Theory	22
2.1.2 Dynamic Scattering Theory: Multislice Theory	25
2.2 CBED, STEM & Scanning CBED	29
2.2.1 CBED	29
2.2.2 STEM	31
2.2.3 Scanning CBED	35

2.3	STEM Simulation.....	36
2.3.1	Elastic Part of STEM Simulation	37
2.3.2	TDS Part of STEM Simulation	38
Chapter 3 Calculation Methods		41
3.1	First Principle Calculation.....	42
3.2	Probe Simulation.....	44
3.3	CBED/STEM Simulation	45
Chapter 4 Results of Calculations.....		47
4.1	Si 100 Direction	47
4.2	Si 110 Direction.....	53
4.3	STO 100 Direction	57
Chapter 5 Conclusions		59
Chapter 6 References.....		60
국문초록		63
감사의글		65

List of Tables

Table 1	Objective aperture size dependence on longitudinal resolution for $E_0=200\text{kV}$ electron	12
Table 2	Optimized parameters of the electron probe in CTEM/Cs-corrected TEM	44

List of Figures

Figure 1	Coordinate system for Huygens-Fresnel principle.....	2
Figure 2	Fraunhofer diffraction of a circular aperture: Airy pattern.....	3
Figure 3	Image resolution limit due to Airy disk	4
Figure 4	Impact of spherical aberration on the electron probe	7
Figure 5	Impact of chromatic aberration on the electron probe	8
Figure 6	Impact of effective source size on the electron probe	9
Figure 7	Effect of four contributions on the probe size in conventional STEM equipped with field-emission gun: $C_s=1\text{mm}$, $C_c=1\text{mm}$, $E_0=200\text{kV}$, $\lambda=0.00251\text{nm}$, $\Delta E=1\text{eV}$, $\delta_{\text{geo}}=0.05\text{nm}$	10
Figure 8	Effect of four contributions on the probe size in Cs-corrected STEM equipped with cold field-emission gun: $C_s=0.005652\text{mm}$, $C_c=1\text{mm}$, $E_0=200\text{kV}$, $\lambda=0.00251\text{nm}$, $\Delta E=0.5\text{eV}$, $\delta_{\text{geo}}=0.05\text{nm}$...	11
Figure 9HADDF-STEM image of Pt atoms dispersed on the $\gamma\text{-Al}_2\text{O}_3$ support: (A) Raw image (B) Bandpass-filtered image. X and Y,Z indicate trimer and dimer, respectively	14
Figure 10	HADDF-STEM image of Sb atoms in the Si crystal.....	15
Figure 11	HADDF-STEM image of Bi atoms in the Si crystal.Two example line scan are shown.....	16
Figure 12	Schematic diagram of gate dielectric device and through-focal series acquisition of HADDF-STEM. A Hf atom appears in the white circles from $\Delta f=-0.5\text{nm}$ to $\Delta f=1.5\text{nm}$	17
Figure 13	Example of strain contrast: the interface between A-Si/C-Si	19
Figure 14	Schematic diagram of crystal in multislice theory. A crystal is regarded as a set of phase objects	26
Figure 15	Schematic diagram of propagation between phase objects. (x',y')	

	is the coordinates of scattering and (x,y) is the coordinates of observation.....	27
Figure 16	Schematic diagram of HADDF STEM imaging. $\psi_p(b), \psi_p(k)$ is the wave function of probe in the real space and reciprocal space. $\psi_t(b), \psi_t(k)$ is the exit wave function in the real space and reciprocal space.....	33
Figure 17	Summary of calculation methods	41
Figure 18	Structure model for the relaxation using the first principle calculations.....	43
Figure 19	Structure model for CBED/STEM simulation: Si 100, Si 110.....	46
Figure 20	Relaxed structure of boron dopant, vacancy and surface roughness (Si 100 direction)	48
Figure 21	Azimuthal integration of CBED for boron dopant, vacancy and surface roughness (Si100 direction)	49
Figure 22	Line scan of simulated STEM image (considering both elastic contribution and inelastic contribution): the center column is the defected column. (Si 100 Direction)	51
Figure 23	Line scan of simulated STEM image (considering just elastic contribution): the center column is the defected column. (Si 100 Direction)	52
Figure 24	Relaxed structure of boron dopant, vacancy and surface roughness (Si 110 direction)	53
Figure 25	Azimuthal integration of CBED for boron dopant, vacancy and surface roughness (Si110 direction)	54
Figure 26	Line scan of simulated STEM image (considering both elastic contribution and inelastic contribution): the right column among center two columns is the defected column. (Si 110 direction)	55
Figure 27	Line scan of simulated STEM image (considering just elastic contribution): the right column among center two columns is the	

	defected column. (Si110 direction)	56
Figure 28	Relaxed structure of oxygen vacancy in TiO column and surface roughness (STO 110 direction)	57
Figure 29	Azimuthal integration of CBED for oxygen vacancy in TiO column and surface roughness (STO 100).....	58

Chapter 1. Introduction

1.1 Resolution Limit of Optical Microscopy

From a long time ago, people have endeavored to know the micro-structure of objects or samples that cannot be seen with a human eye. This curiosity has led the development of microscopes, instruments to magnify objects from tens of times to thousands of times using lens, and people have naturally kept trying to improve the resolution of microscopes. However, there is an intrinsic resolution limit, diffraction limit, because waves determined by the aperture always make the diffracted patterns. This resolution limit is directly related to the motive to develop electron microscopy. In this chapter, diffraction patterns formed by the aperture and limitations of optical microscopes will be discussed in details.

Diffraction is a macroscopic phenomenon that occurs when waves are scattered by the obstacles such as a slit, aperture or grating. Diffraction can be approximated into Fresnel diffraction and Fraunhofer diffraction. Fresnel diffraction and Fraunhofer diffraction are used for describing the near-field diffraction and the far-field diffraction, respectively. These two different kinds of diffraction are derived from Huygens-Fresnel principle which states how waves propagate. (Huygens-Fresnel principle will be treated with the considerable detail in Chapter 2.1.2) Specifically, Huygens-Fresnel principle is mathematically expressed as

$$\psi(x, y) = \frac{1}{i\lambda} \iint q(x', y') \frac{e^{iK\rho'}}{\rho'} \cdot \frac{1}{2} (1 + \cos\theta) dx' dy' \quad (1)$$

where $\mathbf{b} = (x, y)$ is the coordinate of the observation point, $\mathbf{b}' = (x', y')$ is coordinate of the source and $\boldsymbol{\rho}' = \mathbf{b} - \mathbf{b}' + \Delta z$ is the displacement between the source and the observation point. We can derive the mathematical expression of Fraunhofer diffraction from Equation (1) by assuming that the distance between the source and the observation plane is effectively infinite. Under this assumption, the distance $\boldsymbol{\rho}'$ can be simplified and the incline factor $A(\theta) = 1/2(1 + \cos\theta)$ can be neglected out to the integral. Consequently, the waves at the observation point are expressed as

$$\begin{aligned}\psi(x, y) &= \frac{1}{2i\lambda}(1 + \cos\theta) \frac{e^{iK\rho'_0}}{\rho'_0} \iint q(x', y') e^{i(\mathbf{K}-\mathbf{K}_0)\cdot\mathbf{b}'} dx' dy' \\ &= C \iint q(x', y') e^{i(\mathbf{K}-\mathbf{K}_0)\cdot\mathbf{b}'} dx' dy' \quad (2)\end{aligned}$$

where $\boldsymbol{\rho}'_0 = \mathbf{b} + \Delta z$ is the displacement between the origin of source plane and the observation point. This is just the Fourier transform of the object function. (Detailed deviation is well described in the reference, Diffraction Physics, written by J.M Cowely.¹⁾) Equation (2) indicates that diffracted waves through Fraunhofer diffraction are definitely equivalent with the scattered waves derived from the first Born approximation.

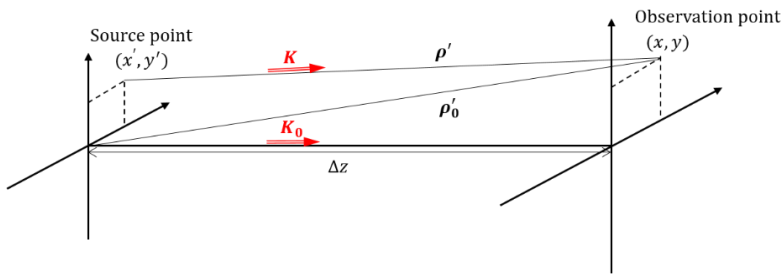


Figure 1. Coordinate system for Huygens-Fresnel principle.

Let's consider the diffraction of a circular aperture. Applying the circular aperture to Equation (2), the diffracted waves are expressed as

$$\psi(x, y) = C \int_{aperture} e^{i(K-K_0) \cdot b'} dA' \quad (3)$$

When y' is chosen as the variable of integration and the radius of a circular aperture is written as R , the waves can be approximated into

$$\psi(x, y) = C \int_{-R}^R e^{iKy' \sin \theta} 2\sqrt{R^2 - y'^2} dy' \quad (4)$$

Substituting $KR \sin \theta$ and y'/R as ξ and u , this integral becomes standard integral of the 1st order Bessel function.

$$\psi(x, y) = 2CR^2 \int_{-1}^1 e^{i\xi u} \sqrt{1 - u^2} du = \pi CR^2 \frac{2J_1(\xi)}{\xi} \quad (5)$$

As a result, the intensity of the diffraction pattern is

$$I = I_0 \left(\frac{2J_1(\xi)}{\xi} \right)^2 \quad (6)$$

This pattern is called Airy pattern and the bright central area is called Airy disk.

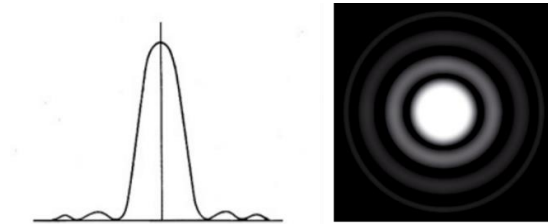


Figure 2. Fraunhofer diffraction of a circular aperture: Airy pattern

Since the first zero of the 1st order Bessel function is 3.832, the angular radius of the first dark ring is

$$\sin\theta = \frac{3.832}{kR} = \frac{0.61\lambda}{R} \quad (7)$$

where R is the radius of the aperture and λ is the wavelength of the wave. Actually, the finite sized lens naturally makes an effect of a circular aperture, so that the diffraction by the lens is unavoidable in the microscope as far as the lens is used for magnification. Therefore, the diffraction by the lens usually acts as a resolution limit in the microscopic images. In other words, two points on the focal plane should be separated larger than the radius of Airy disk in order to be resolved.

$$\Delta x = \frac{0.61\lambda}{D/f} \approx \frac{0.61\lambda}{\alpha} \quad (8)$$

This condition is known as Rayleigh criterion. This indicates that optical microscopes cannot help having the intrinsic resolution limit because of the diffraction. For 500nm blue light, the best resolution would be about $0.3\mu m$ even if the aperture size is assumed to be enough large comparable to the focal length ($D/f \approx 1$).

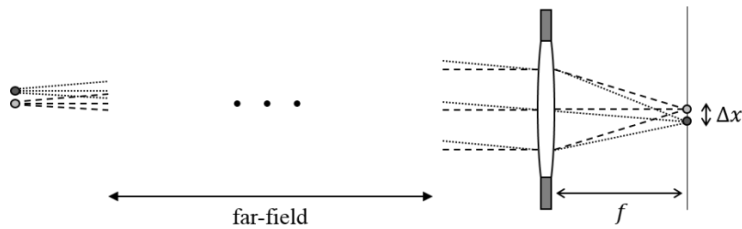


Fig3. Image resolution limit due to Airy disk

Therefore, a new type of waves with short wavelength is necessary to be introduced for the improvement of resolution. The good alternative was a high energy electron. For instance, the electron accelerated to 200kV has a 0.025\AA wavelength, which means that the best resolution would be 0.016\AA . This expectation for the better resolution has led to the development of the electron microscopes.

1.2 Resolution of STEM

Scanning Transmission Electron Microscopy (STEM) is the imaging technique that provides direct structural information as the electron probe scans materials. In STEM, both lateral and longitudinal resolution are determined by the electron probe, of which the dimension is affected not only by aperture size but also by spherical aberration, chromatic aberration and source size. Actually, these four factors are so interrelated that these contributions should be coincidentally considered to estimate the probe dimension. However, it is instructive to investigate each individual contribution using geometrical treatment. Wave optical treatment which can describe the combined effects of the four factors will be discussed together with other theories of STEM in Chapter 2.2.

1.2.1 Lateral Resolution of STEM

It is unavoidable that electrons passing through the aperture show diffraction patterns, since the electrons also have wave characteristics like light. This influences size of the electron probe. The radius of the probe blurred by the diffraction can be described with Rayleigh criterion

$$\delta_D = \frac{0.61\lambda}{\alpha} \quad (9)$$

where α is the convergence angle.

The probe dimension is also affected by lens aberration; spherical aberration and chromatic aberration. Spherical aberration is the phenomenon that electron waves passing through the path far from the optic axis are focused closer than Gaussian focal plane since the magnetic force at the edge side of lens is stronger than that of the center. Gaussian focal plane indicates the plane that electron waves running along the optic axis are focused. As a result of spherical aberration, point source will make a broad disk on Gaussian focal plane. In fact, there is a minimum-sized disk in a certain distance in front of Gaussian focal plane. The blurred effect to the radius of probe by spherical aberration is defined using the minimum-sized disk, which is called the disk of least confusion.

$$\delta_s = \frac{1}{4} C_s \alpha^3 \quad (10)$$

We can move the focal plane to the site of the disk of least confusion by modifying the defocus.

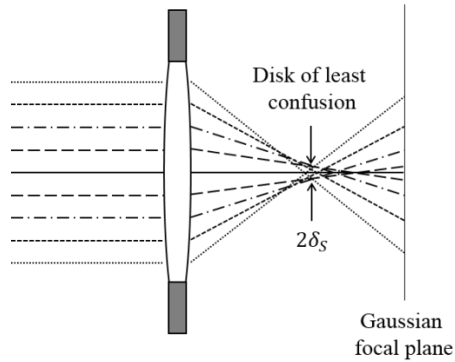


Figure 4. Impact of spherical aberration on the electron probe

Chromatic aberration occurs since electrons with different energies are focused on the different focal plane. If E_0 is the standard energy, the electrons with larger energy than E_0 are focused closer than Gaussian focal plane and the electrons with smaller energy than E_0 are focused further than Gaussian focal plane. The radius of probe with chromatic aberration is defined using the disk size on the Gaussian focal plane.

$$\delta_c = C_c \alpha \frac{\Delta E}{E_0} \quad (11)$$

The radius increases with energy spreading.

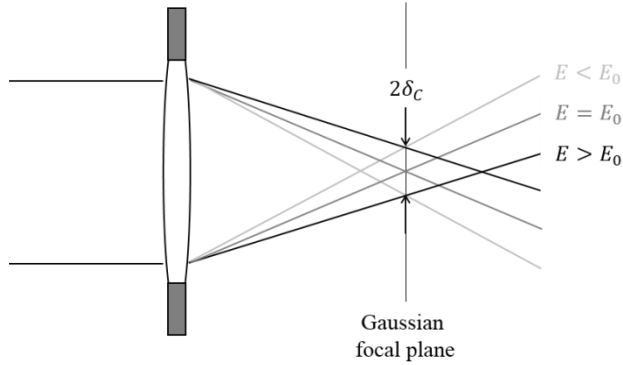


Figure 5. Impact of chromatic aberration on the electron probe

The size of the electron source is another critical factor for the probe dimension. The wave front coming into the lens can be approximated to the plane wave since the source is assumed to exist at the infinite distance from the lens. This leads the image of the source formed on Gaussian focal plane. For a given demagnification M , the radius of the source is expressed as

$$\delta_{geo} = \sqrt{\frac{I_S M}{\pi \Omega B}} \quad (12)$$

where I_S is total current of the source, Ω is the solid angle that electron emits from the source and B is the brightness of the source. It is worthy to note that the effective size of the source is irrelevant to the convergence angle α .

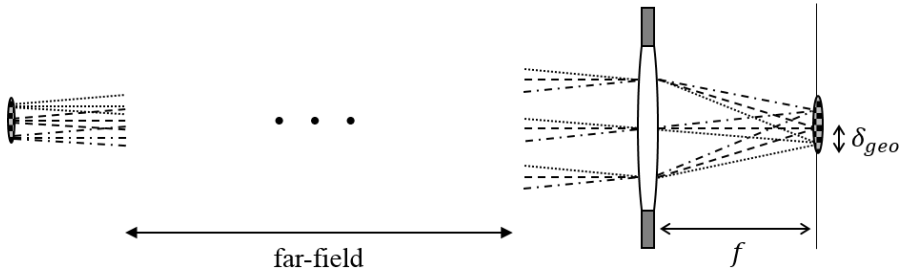


Figure 6. Impact of effective source size on the electron probe

Let's numerically investigate the effects of each factor to the probe

dimension in the conventional TEM by substituting the parameters: Spherical aberration $C_S = 1mm$, Chromatic aberration $C_C = 1mm$, Acceleration Energy $E_0 = 200kV$, Wavelength $\lambda = 0.00251nm$, Energy spreading $\Delta E = 1eV$, and Effective source size $\delta_{geo} = 0.05nm$. Figure 7 shows the probe-size dependence of four factors on the convergence angle α in the log scale. This shows that the dominant limiting factors of the probe radius are the aperture size and the spherical aberration. It would be better to choose a large source size as far as not exceeding the minimum probe size, since the demagnification is directly related with the decrease of beam currents. It is simply estimated that we can have a sub-nanometer scale probe with a conventional TEM, though the geometrical treatment cannot describe the combined effects of the four contributions.

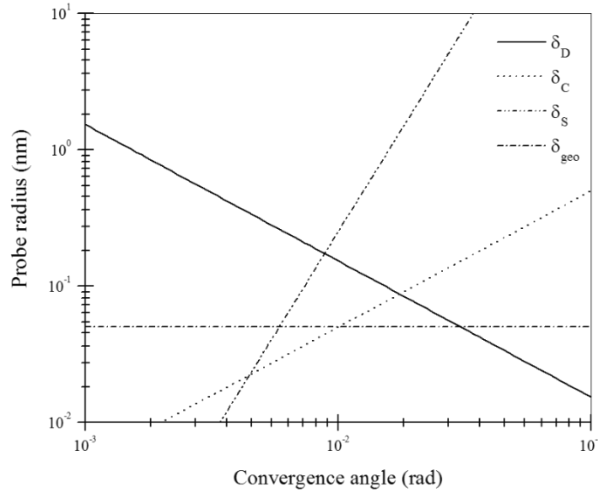


Figure 7. Effects of four contributions on the probe size in conventional STEM equipped with field-emission gun

Let's estimate how the resolution will be improved if spherical aberration corrected lens is used with a cold field-emission gun. (Spherical aberration $C_s = 0.005658mm$, Chromatic aberration $C_c = 1mm$, Acceleration Energy $E_0 = 200kV$, Wavelength $\lambda = 0.00251nm$, Energy spreading $\Delta E = 0.5eV$, Effective source size $\delta_{geo} = 0.05nm$). The correction of spherical aberration is expressed as the parallel shift of spherical aberration contribution in Figure 8 compared with Figure 7. Parallel shift to the right indicates the reduction of the probe size. According to the geometrical interpretation, sub-angstrom scale probe can be obtained if Cs corrected lens is used. Besides, Figure 8 indicates that chromatic aberration would be the limiting factor in Cs-corrected STEM and the source would need to be demagnified for not being the limiting factor.

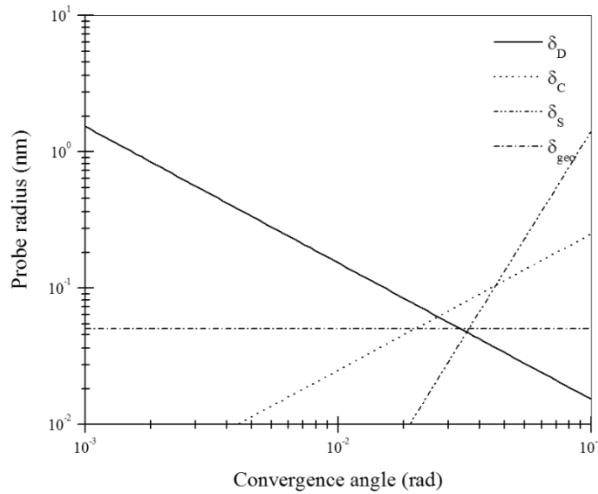


Figure 8. Effects of four contributions on the probe size in Cs-corrected STEM equipped with cold field-emission gun

1.2.2 Longitudinal Resolution of STEM

Since the electron probe is a three dimensional quantity, the depth information as well as the lateral information of the sample can be obtained using STEM. According to the geometrical treatment, the longitudinal resolution² is mainly determined from the aperture size.

$$\Delta z \approx 2 \frac{\lambda}{\alpha^2} \quad (13)$$

Longitudinal resolution according to the different aperture size is listed in Table 1. With the objective aperture used in the conventional STEM (~10mrad), the depth resolution is generally larger than the sample thickness. However, the longitudinal resolution can be reduced to the nanometer scale in Cs-corrected STEM since the optimized probe is obtained with a large objective aperture.

Objective aperture size (α)	Longitudinal resolution (Δz)
10 mrad	50.2 nm
15 mrad	22.3 nm
20 mrad	12.6 nm
25 mrad	8.0 nm

Table 1. Objective aperture size dependence on longitudinal resolution for $E_0 = 200kV$

High depth resolution can be applied to single atomic imaging. Also, high depth resolution could enable 3D reconstruction possible through focal series acquisition of STEM. However, this method has defects that make the lateral extended objects like participation elongated. In principle, this

elongation is unavoidable because 3D optical transfer function always has the missing cone along optic axis³ (the result derived from the wave optical treatment). For instance, the depth resolution would be more than 200nm for 5nm participant.

1.3 Previous Attempts at Point-defect Imaging

The possibility to visualize point defects like dopant atoms with STEM had been raised since HAADF-STEM was proposed to give incoherent images dependent upon atomic number (Z). However, it was practically difficult to realize point-defect imaging because of many restrictions such as sample thickness, signal-to-background ratio and signal-to-noise ratio. The first success to visualize single atoms using HADDF-STEM was platinum (Pt) atoms dispersed on aluminium oxide support ($\gamma - \text{Al}_2\text{O}_3$) by P.D Nellist and S.J Pennycook⁴ (Figure 9). These images were able to be obtained since signal-to-background ratio had been improved due to the reduction of electron probe size. In Figure 9, platinum trimers and dimers can be distinguished through the band-filtered image.

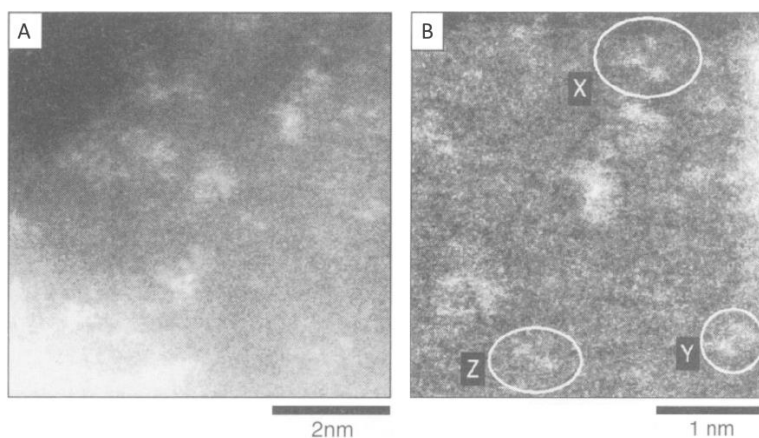


Figure 9. HADDF-STEM image of Pt atoms dispersed on the $\gamma - \text{Al}_2\text{O}_3$ support: (A) Raw image (B) Bandpass-filtered image. X and Y,Z indicate trimer and dimer, respectively⁴.

After the spherical aberration corrector was introduced, probing dopant atoms embedded in the bulk crystal became possible with HADDF-STEM. Antimony (Sb) atoms in a silicon (Si) sample were visualized by P.M Voyle using an aberration-corrected STEM⁵ (Figure 10). It should be noticed that Figure 10 is a processed image. Second order polynomial fit was used for subtracting thickness variation along the wedge, and low pass filter was used for removing scan noise. Non-linear intensity was utilized to highlight the bright spots.

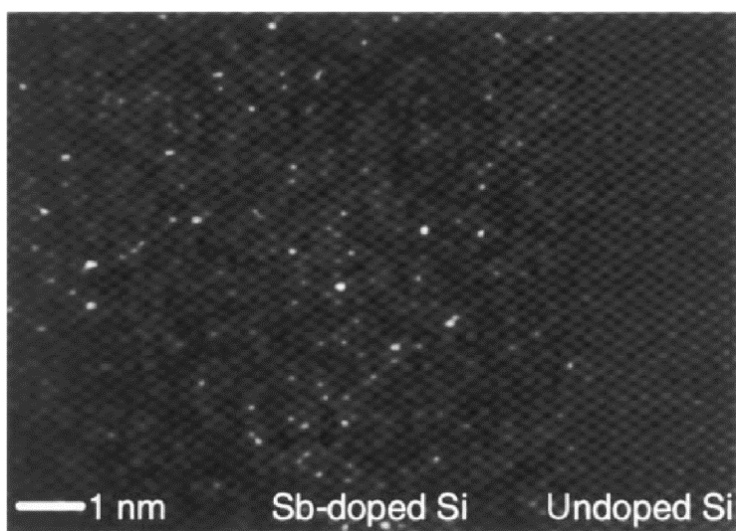


Figure 10. HADDF-STEM image of Sb atoms in the Si crystal⁵.

Imaging bismuth (Bi) atoms in a silicon (Si) sample were subsequently reported by A.R. Lupini⁶ (Figure 11). It is worthy of notice that Figure 11 is the result just by the statistical treatment without any image processing. The column with a bismuth atom is just a little brighter than other columns.

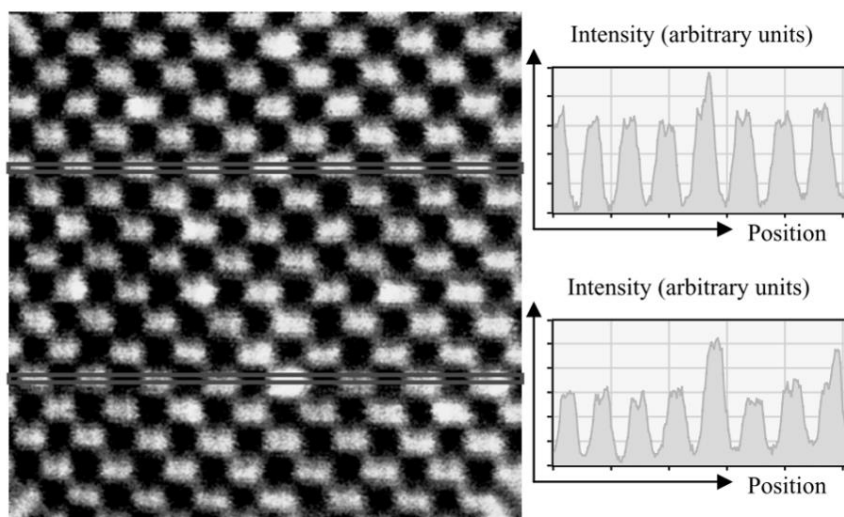


Figure 11. HADDF-STEM image of Bi atoms in the Si crystal⁶.

Two example line scan are shown.

As mentioned in Chapter 1.2.2, another advantage of using spherical aberration corrector is that the large aperture, which leads the small depth of field, can be allowable. The small depth of field allows to observed only limited parts along the beam direction. In this case, the scattering by a single atom can give the significant contribution to the total intensity of a column. According to Equation (13), 300kV acceleration voltage and a 23 mrad aperture provide the 6nm depth of field. Using through-focal series acquisition, K. van Benthem succeeded visualizing Hafnium (Hf) atoms diffused from Hafnium oxide (HfO_2) to a silicon crystal without any image processing⁷ (Figure 12). Furthermore, S.H. Oh directly measured the different configurations of gold (Au) dopant atoms in the silicon nanowire⁸.

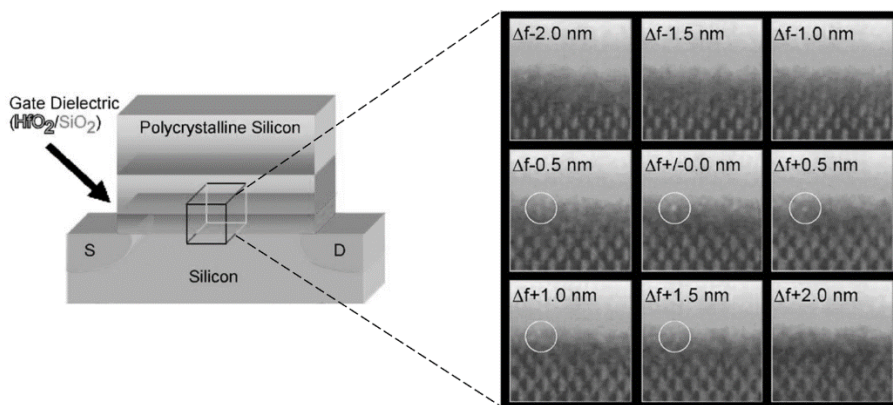


Figure 12. Schematic diagram of gate dielectric device and through-focal series acquisition of HADDF-STEM⁷. A Hf atom appears in the white circles from $\Delta f = -0.5\text{nm}$ to $\Delta f = 1.5\text{nm}$.

Tremendous advances in the realm of point-defect imaging have been made with the states-of-art TEM instruments. However, detecting light dopant atoms or vacancies has not achieved yet. Using HADDF-STEM is not promising since the column with a light dopant atom and a vacancy can be at most 10% darker than other columns. This percentage, 10%, is estimated from Z-contrast scheme proposed by Pennycook when the depth of field is about 5nm. In this situation, a new approach is needed for detecting light dopant atoms or vacancies.

1.4 New Approach for Point-defect Imaging

If defects such as dislocations, dopant atoms or vacancies exist in the crystal, the atoms near the defect will deviate from their original positions. Under this strain field, the scattering of electrons makes a different angular distribution due to the channeling effect as well as the absorption effect. Scattering distribution will cause the extra contrast in ADF STEM, which is called strain contrast. The representative example is the interface between amorphous silicon and crystal silicon.⁹ In Figure 13, the bright band at the interface result from strain contrast. Strain contrast generally shows different aspects depending on experimental condition such as the detector inner angle and the sample thickness, because angular distributions can be easily modified by the experimental condition.

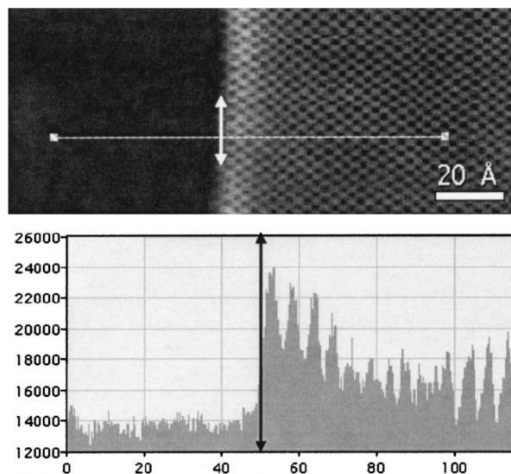


Figure 13. Example of strain contrast: the interface between A-Si/C-Si⁹

We expect that utilization of strain field is a promising solution to overcome the limitation of existing methods for point-defect imaging. Even though strain field generated by light dopant atoms and vacancies may not be strong enough to modify the angular distribution significantly, strained columns can be distinguished from the non-strained ones in a specific angular ranges. If we carry out the imaging only with electrons which are scattered toward that angular region, we expect that light dopant atoms and vacancies can be visualized.

Here, we have studied the feasibility of detecting light dopant atoms and vacancies with strain effects through the computer simulation. The strain field is simulated by structural relaxations with the first principle calculations and the propagation of electron waves is simulated with the multislice calculation, one of the dynamic scattering theory. Specifically, boron dopants and vacancies in silicon and oxygen vacancies in strontium titanate are investigated in this study. We hope this study provide a clue for visualizing a light impurity atom or a vacancy.

Chapter 2. Theoretical Background

2.1 Scattering Theory

Diffraction and scattering have been studied in the field of optics and quantum mechanics from a long time ago. However, these two terms actually indicate the same physical phenomena and derive the same result. Diffraction is just a macroscopic view of scattering process between waves and matters. This ordinary formalism for description of diffraction and scattering is called kinematic theory. Kinematic theory can lead to the position of Bragg conditions, and also describe various influences on electron diffractions such as the crystal structure or the external crystal size. However, kinematic theory is insufficient to describe electron diffractions quantitatively unlike x-ray diffractions or neutron diffractions since the interactions between electron waves are much stronger than those between other particles. The strong interaction between electron waves such as channeling and multiple scattering should be considered for the quantitative analysis of electron diffraction. This is called dynamic scattering effects and the theory that contains these effects is named as dynamic theory. Many calculation methods which include dynamic scattering effects are proposed. Among them, two representative approaches are Bloch method and the multislice method. These dynamic theories are used for the quantitative simulation of HREM, CBED or STEM. In this chapter, we will discuss the ordinary scattering theory, kinematic theory, and the multislice theory, one of dynamic theories.

2.1.1 Kinematic Scattering Theory

Scattering Process is inherently a time-dependent process. However, it is not needed to solve a full time-dependent scattering in order to calculate physically important quantities. Scattering cross-section by fast electrons can be estimated with just time-independent solutions at asymptotic regions. At the asymptotic regions, scattering is dominated by the time-independent Schrodinger equation

$$\left[-\frac{\hbar^2}{2m} \nabla^2 + eV(\mathbf{r}) \right] \psi_k(\mathbf{r}) = E_k \psi_k(\mathbf{r}); \quad E_k = \frac{\hbar^2 k^2}{2m} \quad (14)$$

where the interaction potential $V(\mathbf{r})$ between the incident particle and the target vanishes as $r \rightarrow \infty$ and an incident particle far away from the target is represented as $\phi_k(\mathbf{r}) = (2\pi)^{-3/2} e^{ik \cdot \mathbf{r}}$. The full scattering wave function at asymptotic regions can be simply approximated

$$\psi_k \xrightarrow{r \rightarrow \infty} \frac{1}{(2\pi)^{3/2}} \left(e^{ik \cdot \mathbf{r}} + \frac{f(\theta, \varphi)}{r} e^{ik \cdot \mathbf{r}} \right) \quad (15)$$

where $f(\theta, \varphi)$ is called scattering amplitude, the square of which equals differential scattering cross-section. In fact, the exact solution can be obtained using Green's function $G(\mathbf{r}, \mathbf{r}') = -e^{ik|\mathbf{r}-\mathbf{r}'|}/4\pi|\mathbf{r}-\mathbf{r}'|$.

$$\psi_k = \frac{1}{(2\pi)^{3/2}} \left(e^{ik \cdot \mathbf{r}} - \frac{(2\pi)^{3/2}}{4\pi} \cdot \frac{2me}{\hbar^2} \int d\mathbf{r}' \frac{e^{ik|\mathbf{r}-\mathbf{r}'|}}{|\mathbf{r}-\mathbf{r}'|} V(\mathbf{r}') \psi_k(\mathbf{r}') \right) \quad (16)$$

If we consider the behavior of the exact solution at asymptotic regions, the analytic expression of the scattering amplitude becomes

$$\psi_k \xrightarrow{r \rightarrow \infty} \frac{1}{(2\pi)^{3/2}} \left(e^{i\mathbf{k}\cdot\mathbf{r}} - \frac{(2\pi)^{3/2}}{4\pi} \cdot \frac{2me}{\hbar^2} \int d\mathbf{r}' \frac{e^{i\mathbf{k}\cdot\mathbf{r}}}{r} e^{-i\mathbf{k}\cdot\mathbf{r}^{-1}\cdot\mathbf{r}'} V(\mathbf{r}') \psi_k(\mathbf{r}') \right) \quad (17)$$

$$f(\theta, \varphi) = -\frac{(2\pi)^{\frac{3}{2}}}{4\pi} \cdot \frac{2me}{\hbar^2} \int d\mathbf{r}' e^{-i\mathbf{k}'\cdot\mathbf{r}'} V(\mathbf{r}') \psi_k(\mathbf{r}') \quad (18)$$

However, it should be noticed that the wave function $\psi_k(\mathbf{r}')$ is included in the integrand, which means that iterative calculations are needed to obtain the exact scattering amplitude. If the wave function in the integrand is assumed to be a plane wave $\phi_k(\mathbf{r}) = (2\pi)^{-3/2} e^{i\mathbf{k}\cdot\mathbf{r}}$, the scattering amplitude can be summarized into the Fourier transform of the interaction potential $V(\mathbf{r})$.

$$f(\theta, \varphi) = -\frac{m}{2\pi\hbar^2} \int d\mathbf{r}' e^{-i(\mathbf{k}'-\mathbf{k})\cdot\mathbf{r}'} V(\mathbf{r}') \quad (19)$$

This is the first (order) Born approximation. When the incident particle energy is much higher than the interaction potential $V(\mathbf{r})$, the differential scattering cross-section is good enough to be described with the first Born approximation. Therefore, high energy particle scatterings like x-ray scattering and neutron scattering have been studied using the first Born approximation.

Let's consider scattering of a periodic crystal using the first Born approximation. Under the rigid-body approximation, the potential of a crystal is assumed to be the superposition of atomic potentials. Bonding effects are neglected in the rigid-body approximation.

$$V(\mathbf{r}) = \sum_n \sum_{\alpha} V_{\alpha}(\mathbf{r} - \mathbf{R} - \mathbf{r}_{\alpha}) \quad (20)$$

where n is the index of unit cell and α is the index of atom in the unit cell. According to the first Born approximation, the scattering amplitude is the Fourier transform of the interaction potential

$$\begin{aligned}
f(\theta, \varphi) &= -\frac{m}{2\pi\hbar^2} \int d\mathbf{r}' \sum_n \sum_{\alpha} V_{\alpha}(\mathbf{r}' - \mathbf{R}_n - \mathbf{r}_{\alpha}) e^{-i\mathbf{u} \cdot \mathbf{r}'} \\
&= -\frac{m}{2\pi\hbar^2} \sum_n e^{-i\mathbf{u} \cdot \mathbf{R}_n} \sum_{\alpha} \int d\mathbf{r} V_{\alpha}(\mathbf{r}) e^{-i\mathbf{u} \cdot \mathbf{r}} e^{-i\mathbf{u} \cdot \mathbf{r}_{\alpha}} \\
&= -\frac{m}{2\pi\hbar^2} \frac{1}{\Omega} \sum_{\mathbf{g}} \delta(\mathbf{u} - \mathbf{g}) \sum_{\alpha} f_{\alpha}(\mathbf{g}) e^{-iM_{\alpha}g^2/4} e^{-i\mathbf{g} \cdot \mathbf{r}_{\alpha}} \quad (21)
\end{aligned}$$

where Ω is the volume of unit cell and $e^{-iMg^2/4}$ is called Debye-Waller factor. In deriving Equation (21), Dirac comb function is used $\sum_n \delta(\mathbf{u} - \mathbf{g}) = \sum_n e^{-i\mathbf{u} \cdot \mathbf{R}_n}$, where \mathbf{g} is the reciprocal lattice vector. This Dirac comb function allows only reflections which satisfy the Bragg condition $\mathbf{k} - \mathbf{k}' = \mathbf{g}$. $f_{\alpha}(\mathbf{u})$ is called the atomic scattering factor, which is the Fourier transform of isolated atomic potential, and $\sum_{\alpha} f_{\alpha}(\mathbf{u}) e^{-i\mathbf{u} \cdot \mathbf{r}_{\alpha}}$ is called geometrical structure factor of crystal, which indicates the intensity of Bragg reflections. Thermal vibrations are considered by Debye-Waller factor. It can be derived using the property $\langle e^A \rangle = e^{\langle A^2 \rangle / 2}$ as

$$\langle e^{-i\mathbf{u} \cdot (\mathbf{r}_{\alpha} + \mathbf{u}_{\alpha})} \rangle = e^{-i\mathbf{u} \cdot \mathbf{r}_{\alpha}} \cdot \langle e^{-i\mathbf{u} \cdot \mathbf{u}_{\alpha}} \rangle = e^{-i\mathbf{u} \cdot \mathbf{r}_{\alpha}} \cdot e^{-\frac{1}{2} \langle (\mathbf{u}_{\alpha})^2 \rangle u^2} = e^{-i\mathbf{u} \cdot \mathbf{r}_{\alpha}} e^{-\frac{1}{4} M_{\alpha} u^2}$$

where \mathbf{u}_{α} is the time-dependent displacement of α atom. Therefore, Debye-Waller factor can be interpreted as a factor to reduce the elastic scattering power due to thermal vibrations.

2.1.2 Dynamics Scattering Theory: Multislice Theory

Multislice theory is one of calculation methods to consider dynamic scattering effects. At first, multislice theory was suggested from physical optics approach by Cowley and Moodie¹⁰. They assumed that a crystal is a set of two dimensional phase objects and transmission through the crystal is described as a repeat of phase shift by phase objects and propagation in the vacuum. In fact, it is possible to describe the effects of the crystal on the transmission electrons with a just phase shift, since these electrons are nearly deflected by the crystal. This is because transmission electrons have enough high energy with respect to the crystal potential. This is called phase object approximation.

With transmission electron energy $E = eU_0$ and the crystal potential $V(\mathbf{r})$,

$$K_{eff} = \frac{(2m)^{\frac{1}{2}}}{\hbar} (E + eV(\mathbf{r}))^{\frac{1}{2}} \approx \frac{2\pi}{\lambda} \left(1 + \frac{V(\mathbf{r})}{2U_0} \right) \quad (22)$$

The phase shift of electron wave experienced in the crystal is

$$\int_{z_n}^{z_n+\Delta z} dz 2\pi \left(\frac{1}{\lambda_{eff}} - \frac{1}{\lambda} \right) \approx \frac{\pi}{\lambda U_0} \int_{z_n}^{z_n+\Delta z} dz V(\mathbf{r}) = \sigma V(\mathbf{b}) \quad (23)$$

where \mathbf{b} is a two dimensional position vector. Therefore, the effect of the crystal potential on the transmission electrons can be simply considered through multiplying $e^{i\sigma V(\mathbf{b})}$ to the incident electron waves. The function $Q_{nc}(\mathbf{b}, \Delta z) = e^{i\sigma V(\mathbf{b})}$ is called phase grating function or phase object.

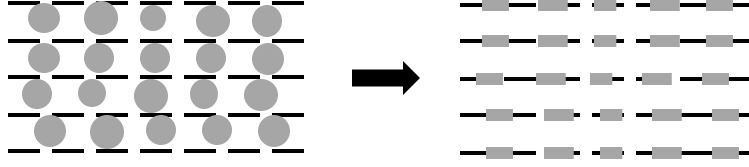


Figure 14. Schematic diagram of crystal in multislice theory. A crystal is regarded as a set of phase objects

Between the phase objects, electron propagation can be described by Huygens principle. Huygens principle states how waves propagate: Every point on the wave front will be a point source for secondary spherical waves and another wave front is constructed by interference of near-by secondary spherical waves. About two centuries later after proposing Huygens principle, Fresnel experimentally found that secondary waves should have phase shift by $1/i\lambda$ with respect to the incident wave and be multiplied the incline factor $A(\theta) = 1/2(1 + \cos\theta)$. The incline factor $A(\theta)$ makes electron amplitude have maximum value on the forward direction and minimum value on the back scattered direction. With applying this Huygens-Fresnel principle to our case, the electron waves reaching another phase object are expressed as

$$\psi(\mathbf{b}, z_{n+1}) = \frac{1}{i\lambda} \int d\mathbf{b}' \psi(\mathbf{b}', z_n) \frac{e^{iK\rho'}}{\rho'} \cdot \frac{1}{2} \left(1 + \frac{\boldsymbol{\rho}' \cdot \mathbf{z}}{\rho' z} \right) \quad (24)$$

where $\boldsymbol{\rho}'$ is the displacement between the initial point, i.e. point source, and the final point: $\boldsymbol{\rho}' = \mathbf{b}' - \mathbf{b} + \Delta\mathbf{z}$.

Since transmission electrons are nearly deflected as previously mentioned, we can modified Equation (24) to the simplified form. This is

called the small-angle scattering approximation.

$$\begin{aligned}\psi(b, z_{n+1}) &= e^{iK\Delta z} \int d\mathbf{b}' \psi(b, z_n) \frac{e^{iK|\mathbf{b}' - \mathbf{b}|^2/2\Delta z}}{i\lambda\Delta z} \\ &= e^{iK\Delta z} \psi(b, z_n) \otimes P(\mathbf{b}, \Delta z) \quad (25)\end{aligned}$$

Therefore, the electron waves reaching another phase object can be simply expressed as a convolution of the waves on the previous phase object and the propagation function $P(\mathbf{b}, \Delta z)$.

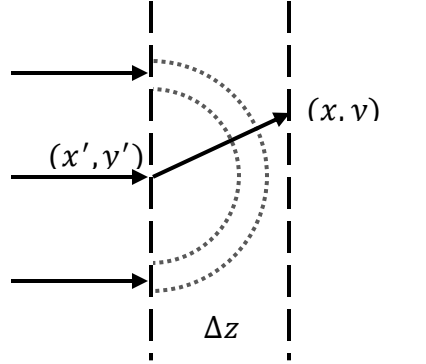


Figure 15. Schematic diagram of propagation between phase objects. (x', y') is the coordinates of scattering and (x, y) is the coordinates of observation.

In multislice theory, the electron waves after the n_c th crystal slice are summarized into

$$\psi(\mathbf{b}, z_{n_c+1}) = \{\psi(\mathbf{b}, z_{n_c}) Q_{n_c}(\mathbf{b}, \Delta z)\} \otimes P(\mathbf{b}, \Delta z) \quad (26)$$

and this process is repeated until the electron waves leave the crystal. Quantum mechanically, this multislice equation was also derived directly from Schrodinger equation by Ishizuka¹¹ and derived using Feynman's path-integral scheme by Van Dyck¹².

2.2 CBED, STEM & Scanning CBED

2.2.1 CBED

CBED (Convergent Beam Electron Diffraction) is the electron

diffraction technique obtained by converging electron beam onto the sample. Diffraction patterns generated by the electron probe give totally different kinds of information depending upon condenser apertures and convergence angles. For very large convergence angle, if the specific diffracted disk is recorded with the selected-area aperture and defocus, it is specially called LACBED (Large Angle Convergent Beam Electron Diffraction). For the small convergence angle, if diffraction pattern similar to SAED (Selected-Area Electron Diffraction) is obtained, it is called electron nano-diffraction named by Cowley¹³, which have been widely used in analyzing nano-sized materials like nano particles or nano rod. We will only focus on the diffraction patterns using medium convergence angle described as CBED. Actually, CBED is one of the oldest electron diffraction technique proposed by Kossel and Mollenstedt¹⁴. This technique has continuously been developing along the advancement of TEM. The biggest change is the size of electron probe. Since thermionic source like LaB₆ is a spatially incoherent source, the lateral coherence cannot help restricting the size of electron probe. For obtaining the nm-order probe with the thermionic source, it needs several hundred times of demagnification than the field-emission gun. In practice, CBED using thermionic source is generally the result of the μm -size electron probe. In contrast, the sub nm-size electron probe can be easily obtained by the field-emission gun. In the field-emission TEM, the sample volume in CBED is usually determined by electron propagation as well as by the probe size. Moreover the size of electron probe became the sub angstrom order as C₃ spherical aberration was corrected. In the Cs-corrected TEM, CBED gives structure information sensitive to individual atomic column.

While SAED gives structure information just by the Bragg position, CBED provides lots of crystallographic information through the CBED disk.

Symmetry of crystal like point group symmetry or space group symmetry can be determined with CBED. Stain of crystal can also be measured by measuring lattice parameters or unit cell information. Besides, CBED can be used for the sample thickness measurement. Sometimes, defects like dislocations and planar defects are analyzed with CBED. Another advantage of CBED is that the nm-scale area can be analyzed with CBED, since the observed area is determined by the size of electron probe. However, there is also shortcoming in the CBED technique. The sample can be easily damaged or contaminated compared with other TEM techniques, since tons of electrons are focused into the small area in CBED.

2.2.2 STEM

When the nm-size electron probe is focused on the sample, differential scattering cross-section varies with the observing position. When electrons scattered into the specific angle range are collected while the probe scans the material, we can obtain the image which contains structure information. This imaging technique is called STEM. STEM can be separated into BF-STEM

and ADF-STEM according to the detection angle. BF-STEM makes use of a small detector on the optic axis and ADF-STEM uses the annular-type detector that collect electrons scattered into the large angles. We will only focus on ADF-STEM.

There are two primary sources for generating high-angle scattering. One is Rutherford scattering, which is the asymptotic behavior of the elastic scattering. We can check the asymptotic behavior of electron scatterings through the following consideration. As we have known from chapter 2.1.1, the (elastic) scattering amplitude of electron is the Fourier transform of the potential. Similarly, the scattering amplitude of X-ray is the Fourier transform of the electron charge density.

$$f^e(\mathbf{u}) = \int d\mathbf{r} e^{-i\mathbf{u}\cdot\mathbf{r}} V(\mathbf{r}) \quad (19)'$$

$$f^x(\mathbf{u}) = \int d\mathbf{r} e^{-i\mathbf{u}\cdot\mathbf{r}} \rho(\mathbf{r}) \quad (27)$$

Potential is correlated with the electron charge density by Poisson equation.

$$\nabla^2 V(\mathbf{r}) = -\frac{e}{4\pi\epsilon_0} [Z_0\delta(\mathbf{r}) - \rho(\mathbf{r})] \quad (28)$$

Taking the Fourier transform of Equation (28) with the scattering amplitude of electron and x-ray (Equation (19)', Equation (27))

$$f^e(\mathbf{u}) = \frac{e}{4\pi\epsilon_0} \frac{[Z_0 - f^x(\mathbf{u})]}{u^2} \quad (29)$$

This relation is called Mott formula, which shows the relationship between electron scattering factor and x-ray scattering factor. In Mott formula, we can notice that electron scattering converges to Rutherford scattering at the high scattering angle (the asymptotic region). The second source for high-angle scattering is thermal diffuse scattering (TDS). TDS, one of inelastic scatterings, is the result of atomic vibrations in the crystal. TDS introduces small energy loss but large momentum transfer, so TDS is the major inelastic scattering event that affects high-angle scattering among various inelastic scatterings.

Meanwhile, HAADF-STEM (High Angle ADF-STEM) is the widely used technique since it is intuitive incoherent imaging. Incoherent image indicate that there is no phase correlation between two points in the image. Imaging by TDS is inherently incoherent because there is no phase correlation between the inelastic events. Contrary to expectation, imaging by elastic scattering is also incoherent if we collect electrons with a large inner-angle. Let's prove this statement by calculating the intensity of ADF-STEM using the single phase object approximation¹⁵. Let's assume the source is totally coherent and C_3 spherical aberration is not corrected. Then, the wave function of electron probe is expressed

$$\psi_p(\mathbf{b} - \mathbf{b}_0) = \int A(\mathbf{k}) e^{-i\chi(\mathbf{k})} e^{i\mathbf{k} \cdot (\mathbf{b} - \mathbf{b}_0)} d\mathbf{k} \quad (30)$$

where $A(\mathbf{k})$ is aperture function, having a value 1 when $|\mathbf{k}| \leq \mathbf{k}_{max}$, $\chi(\mathbf{k})$ is phase shift due to the aberration, $\chi(\mathbf{k}) = C_s \lambda^3 k^4 / 32\pi^3 + \Delta f \lambda k^2 / 4\pi$, \mathbf{b}

and \mathbf{k} are two dimensional position vector and reciprocal vector. In the phase object approximation, the wave exiting the sample is just multiplication of incident wave $\psi_p(\mathbf{b} - \mathbf{b}_0)$ and phase object function $Q(\mathbf{b})$.

$$\psi_t(\mathbf{b}, \mathbf{b}_0) = \psi_p(\mathbf{b} - \mathbf{b}_0)Q(\mathbf{b}) \quad (31)$$

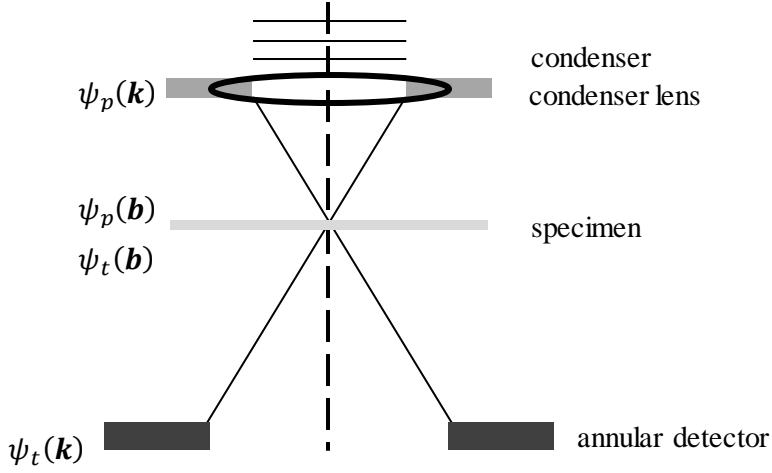


Figure 16. Schematic diagram of DDF STEM imaging.

$\psi_p(\mathbf{b}), \psi_p(\mathbf{k})$ is the wave function of probe in the real space and reciprocal space. $\psi_t(\mathbf{b}), \psi_t(\mathbf{k})$ is the exit wave function in the real space and reciprocal space.

Since ADF-STEM is the technique that collects electrons scattered into the annular detector, the intensity is expressed as

$$\begin{aligned} I_{ADF}(\mathbf{b}_0) &= \int D(\mathbf{k}_f) \times |FT[\psi_p(\mathbf{b} - \mathbf{b}_0)Q(\mathbf{b})]|^2 d\mathbf{k}_f \\ &= \int D(\mathbf{k}_f) \times \left| \int Q(\mathbf{k}_f - \mathbf{k}) \psi_p(\mathbf{k}) e^{-i\mathbf{k} \cdot \mathbf{b}_0} d\mathbf{k} \right|^2 d\mathbf{k}_f \quad (32) \end{aligned}$$

Where $D(\mathbf{k}_f)$ is a detector function. Taking the Fourier transform and using the properties of Dirac delta function $\delta(x' - x) = 1/2\pi \int dk e^{ik(x' - x)}$,

$$I_{ADF}(\mathbf{q}) = \iint D(\mathbf{k}_f) \psi_p(\mathbf{k}) \psi_p^*(\mathbf{k} + \mathbf{q}) \times Q(\mathbf{k}_f - \mathbf{k}) Q^*(\mathbf{k}_f - \mathbf{k} - \mathbf{q}) d\mathbf{k}_f d\mathbf{k}$$

If we assume ADF detector is large enough to neglect aperture overlap region,

$$I_{ADF}(\mathbf{q}) = \int \psi_p(\mathbf{k}) \psi_p^*(\mathbf{k} + \mathbf{q}) d\mathbf{k} \times \int D(\mathbf{k}_f) Q(\mathbf{k}_f) Q^*(\mathbf{k}_f - \mathbf{q}) d\mathbf{k}_f \quad (33)$$

By the Fourier transformation, the intensity of ADF-STEM can be simplified into

$$I_{ADF}(\mathbf{b}_0) = |P(\mathbf{b}_0)|^2 \otimes O(\mathbf{b}_0) \quad (34)$$

where $|P(\mathbf{b}_0)|^2$ is point spread function and $O(\mathbf{b}_0)$ is object function.

Therefore, it is proven that ADF-STEM is incoherent imaging whether intensity comes from elastic scattering or TDS.

2.2.3 Scanning CBED

As the performance of experimental instrument develops, the method of TEM analysis will also be extended. The representative example is scanning CBED, which results from the advancement of CCD (Charge-Coupled Device). These days, CCD is used for quantitative analysis of electron diffraction, since

it can provide a large dynamic range and a great linearity. Furthermore, it becomes possible to record the electron diffraction patterns during scanning the material. Continuous records for CBED pattern in the scanning area provide new techniques for structural analysis with atomic resolution. One simple application of scanning CBED is reemergence of STEM image by integrating diffraction pattern. Also, our scheme for imaging point defect is based upon scanning CBED. In order to analyze the materials using scanning CBED, it is essential to characterize the noise in the scanning CBED. We will discuss the characteristic of the noise in scanning CBED later.

2.3 STEM Simulation

As mentioned above, there are two primary sources for generating the high-angle scattering: Rutherford scattering and TDS. Thus, STEM simulation requires both simulations of elastic scattering and TDS. Elastic scattering can be simulated with the dynamic scattering theories, Bloch method and multislice method. Each method has its own advantages: Bloch method makes physical interpretation simple, but the multislice method reduces a computing burden

for simulating STEM image of defective structure and Cs-corrected STEM image. On the other hands, TDS essentially requires approximations for simulating TDS effects because TDS is a time-dependent incoherent process. Nevertheless, there have been several attempts to include TDS in the dynamic scattering theories. Wang and Cowley directly derived generalized multislice equation including TDS from Yoshioka's coupled equation¹⁶. Loane and Silcox inserted TDS effects in the multislice method using frozen phonon model¹⁷. Ishizuka used absorptive potential to describe TDS influence of HADDF STEM image¹⁸. ZMULT, the code used in our research, is based on the multislice method using the Ishizuka absorptive STEM potential. In the following chapters, we will discuss the elastic scattering with the multislice method and the insertion of TDS effects with Ishizuka method.

2.3.1 Elastic Part of STEM Simulation

In fact, we've already derived the elastic part of STEM simulation in the Chapter 2.2.2. However, the single phase object approximation is not appropriate for the thick samples. The STEM simulation with the multislice method follows the same formalism except for the interaction part between electrons and the sample. As before, the incident wave function of the probe is expressed as

$$\psi_p(\mathbf{b} - \mathbf{b}_0) = \int A(\mathbf{k}) e^{-i\chi(\mathbf{k})} e^{i\mathbf{k} \cdot (\mathbf{b} - \mathbf{b}_0)} d\mathbf{k} \quad (30)'$$

where $\chi(\mathbf{k})$ is phase shift due to the aberration, $\chi(\mathbf{k}) = C_s \lambda^3 k^4 / 32\pi^3 + \Delta f \lambda k^2 / 4\pi$. If more residual aberrations are necessary to be included, the phase shift should be modified into

$$\begin{aligned} \chi(\mathbf{k}) = & C_s \lambda^3 k^4 / 32\pi^3 + \Delta f \lambda k^2 / 4\pi + f_{\alpha 2} \lambda k^2 \sin[2(\phi - \phi_{\alpha 2})] / 4\pi \\ & + f_{\alpha 3} \lambda^2 k^3 \sin[3(\phi - \phi_{\alpha 3})] / 12\pi^2 \\ & + f_{c3} \lambda^2 k^3 \sin[\phi - \phi_{c3}] / 12\pi^2 \end{aligned}$$

where $f_{\alpha 2}$ is twofold astigmatism, $f_{\alpha 3}$ is threefold astigmatism and f_{c3} is coma.¹⁹ As the primary electron pass the sample, the wave function of probe will evolve along the multislice equation (Equation (26)). Thus the wave function at the $(n_c + 1)$ th slice will be expressed as

$$\psi_p(\mathbf{b} - \mathbf{b}_{0, z_{n_c+1}}) = \{\psi_p(\mathbf{b} - \mathbf{b}_{0, z_{n_c}}) Q_{n_c}(\mathbf{b}, \Delta z)\} \otimes P(\mathbf{b}, \Delta z) \quad (26)'$$

and the exit wave function $\psi_t(\mathbf{b} - \mathbf{b}_0)$ equals the wave function of probe evolved to the end.

$$\psi_t(\mathbf{b} - \mathbf{b}_0) = \psi_p(\mathbf{b} - \mathbf{b}_0, d) \quad (35)$$

Since ADF-STEM is the technique to collect electrons scattered into the annular detector, the elastic part intensity of HADDF STEM image is simply expressed as

$$I_{ADF}^{Elastic}(\mathbf{b}_0) = \int D(\mathbf{k}_f) \times |FT[\psi_p(\mathbf{b} - \mathbf{b}_0, d)]|^2 d\mathbf{k}_f \quad (36)$$

2.3.2 TDS Part of STEM Simulation¹⁸

Scattering cross-section of TDS into the specific angle can be approximately calculated from the absorptive potential. Actually, this scheme is first introduced into the Bloch method by Pennycook and Jesson²⁰ and is applied in the multislice equation (Equation (26)) by Ishizuka¹⁸. The only thing modified due to the absorptive potential in the multislice method is the phase grating function $Q_{n_c}(\mathbf{b}, \Delta z)$.

$$Q_{n_c}(\mathbf{b}, \Delta z) = e^{i\sigma[V(\mathbf{b}) + iV^{abs}(\mathbf{b})]} = e^{i\sigma V(\mathbf{b})} e^{-\sigma V^{abs}(\mathbf{b})} \quad (37)$$

Let's investigate how this modification can give the TDS effects in HADDF STEM image. the Fourier transform of output wave function has the following magnitude

$$\begin{aligned} |\psi_p(\mathbf{k}, z_{n_c+1})| &= |FT[Q_{n_c}(\mathbf{b}, \Delta z)\psi_p(\mathbf{b}, z_{n_c+1})] \cdot P(\mathbf{u})| \\ &= |FT[Q_{n_c}(\mathbf{b}, \Delta z)\psi_p(\mathbf{b}, z_{n_c+1})]| \quad (38) \end{aligned}$$

since $FT[P(\mathbf{b}, \Delta z)] = e^{-\pi i u^2 \Delta z \lambda}$.

Applying Parseval's theorem $(\int_{-\infty}^{\infty} \overline{f(x)} f(x) dx = \int_{-\infty}^{\infty} \overline{f(k)} f(k) dk)$ twice in the Equation (38),

$$\begin{aligned} \int |\psi_p(\mathbf{b}, z_{n_c+1})|^2 d\mathbf{b} &= \int |\psi_p(\mathbf{k}, z_{n_c+1})|^2 d\mathbf{u} \\ &= \int |FT[Q_{n_c}(\mathbf{b}, \Delta z)\psi_p(\mathbf{b}, z_{n_c})]|^2 d\mathbf{u} \\ &= \int |Q_{n_c}(\mathbf{b}, \Delta z)\psi_p(\mathbf{b}, z_{n_c})|^2 d\mathbf{b} \quad (39) \end{aligned}$$

Therefore, the loss energy at each slice due to absorptive potential is simply

calculated as

$$\begin{aligned}
I_{n_c} &= \int \left(|\psi_p(\mathbf{b}, z_{n_c})|^2 - |\psi_p(\mathbf{b}, z_{n_c+1})|^2 \right) d\mathbf{b} \\
&= \int |\psi_p(\mathbf{b}, z_{n_c})|^2 \left[1 - e^{-2\sigma V_{n_c}^{abs}(\mathbf{b})} \right] d\mathbf{b} \\
&\approx \int 2\sigma |\psi_p(\mathbf{b}, z_{n_c})|^2 V_{n_c}^{abs}(\mathbf{b}) d\mathbf{b} \quad (40)
\end{aligned}$$

As noticed in this derivation, this absorptive potential scheme cannot describe the redistributions of TDS. However, this will not give an appreciable error if the intensity that fall into the annular detector is just considered. This scheme also approximates that TDS is fully incoherent, so that total TDS part intensity of HADDF STEM image is expressed as the summation of all intensity generated from each slice.

$$I_{ADF}^{TDS}(\mathbf{b}_0) = \sum_{z_{n_c}=0}^d \int 2\sigma |\psi_p(\mathbf{b}, z_{n_c})|^2 V_{n_c}^{abs}(\mathbf{b}) d\mathbf{b} \quad (41)$$

Of course, it is important to construct absorptive potential for TDS scattered electrons toward the annular detector. The ordinary potential is usually reconstructed with atomic scattering factor $f_\alpha(\mathbf{u})$ (rigid-body approximation).

$$V_g = -\frac{1}{\Omega_0} \sum_{\alpha} f_{\alpha}(\mathbf{g}) e^{-\frac{1}{4}M_{\alpha}g^2} e^{-i\mathbf{g}\cdot\mathbf{r}_{\alpha}} \quad (42)$$

(These atomic scattering factors can be calculated through many methods such as Hartree-Fock method²¹). Similarly, the absorptive potential for TDS can be made using the modified absorptive form factor. The modified absorptive form

factor used in this scheme is little different from the absorptive form factor proposed by Hall and Hirsh^{22,23}. Concretely, Hall and Hirsh have interest in TDS for all direction, but TDS directed into the annular detector is only considered in this modified scheme. The modified absorptive form factor for STEM simulation is

$$f_{\alpha}^{abs(HA)}(\mathbf{u}) = \frac{\pi\hbar}{m_0v} \int_{detector} d\sigma(\mathbf{u}') \left(f_{\alpha}(\mathbf{u}') f_{\alpha}(\mathbf{u}' - \mathbf{u}) \left\{ 1 - e^{-\frac{1}{2}M_{\alpha}(\mathbf{u}'^2 - \mathbf{u}' \cdot \mathbf{u})} \right\} \right)$$

This equation indicates that the modified absorptive form factor consists of the usual atomic scattering factors²⁴. Therefore, we can construct the absorptive potential for TDS toward the detector.

$$V_g = -\frac{1}{\Omega_0} \sum_{\alpha} f_{\alpha}^{abs(HA)}(g) e^{-\frac{1}{4}M_{\alpha}g^2} e^{-i\mathbf{g} \cdot \mathbf{r}_{\alpha}} \quad (43)$$

3. Calculation Methods

Strain contrast results from the combination of the channeling effect and the absorption effect under strain field. Therefore, the channeling effect and the strain field due to a point defect should be considered for our study. The first principle calculations based on the density functional theory was carried

out to get relaxed structure and the dynamic scattering calculation based on the multislice theory was conducted for CBED/STEM simulations. Also, the electron probe plays a dominant role in the formation of CBED. Thus, we optimized the electron probe using Simplex algorithms as implemented in PROBE.

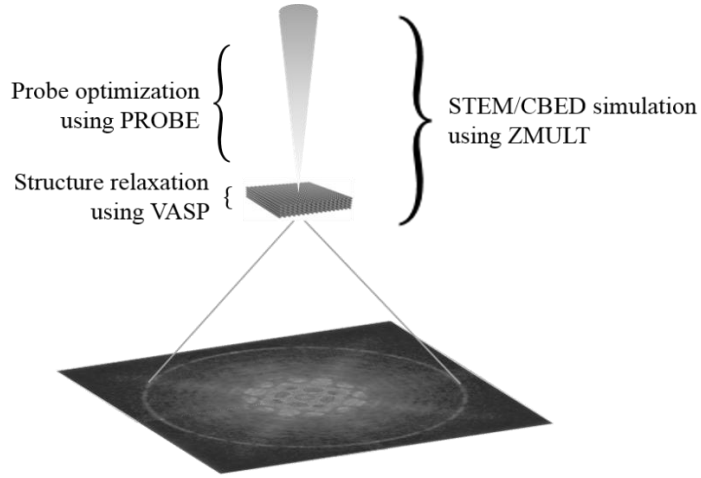


Figure 17. Summary of calculation methods

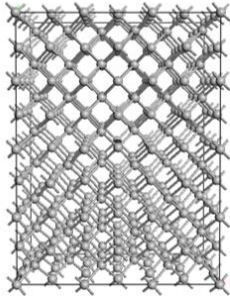
3.1 First Principle Calculations

The first principle calculations based on the density functional theory has been carried out using the VASP²⁵ (Vienna Ab initio Simulation Package) pseudopotential code to obtain relaxed structure containing a defect. We used the local-density approximations for the exchange-correlation functional and ultrasoft pseudopotentials for descriptions of core electrons. Plain-wave basis sets were used with plain-wave cutoff 500eV. Brillouin-zone integrations were

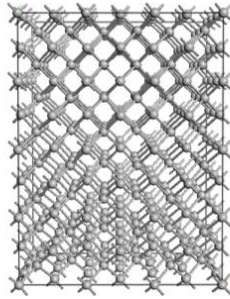
carried out on a grid of $2 \times 2 \times 2$ Monkhorst-Pack special points and on a grid of $2 \times 2 \times 1$ Monkhorst-Pack special points especially for surface structures. We used big-enough unit cell in order that the interaction energy between point defects can be negligible. For Si 100 direction, we used $3 \times 3 \times 4$ Si supercell with a boron dopant or a vacancy positioned on (0.5,0.5,0.5) and $3 \times 3 \times 2$ Si slab with a surface defect. For Si 110 direction, we used $4 \times 2\sqrt{2} \times 2\sqrt{2}$ Si supercell with a boron dopant or a vacancy positioned on (0.5,0.5,0.5) and $4 \times 2\sqrt{2} \times 1\sqrt{2}$ Si slab with a surface defect. Si slab had the vacuum region larger than 15 \AA and the bottommost layer of Si slab was passivated with hydrogen atoms with 1.00 e. The last layers of all side were fixed to be applied into the unit cell of STEM/CBED simulation. Remaining coordinates were relaxed by minimizing the Hellmann-Feynman forces less than 0.02 eV/\AA .

Si 100 direction

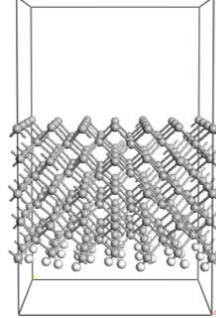
Boron dopant



Vacancy

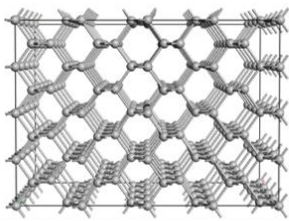


Surface roughness

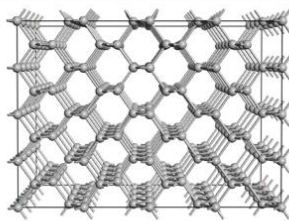


Si 110 direction

Boron dopant



Vacancy



Surface roughness

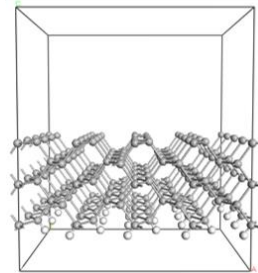


Figure 18. Structure models for the relaxation using the first principle calculations

3.2 Probe Simulation

The electron probe has been optimized in the two conditions using Simplex algorithms as implemented in PROBE. Conventional TEM is dominantly affected by defocus, but Cs-corrected TEM is sensitively influenced by the various residual aberrations like astigmatism or coma. Therefore, just defocus is optimized for the probe of the conventional TEM but two-fold astigmatism, three-fold astigmatism and coma as well as defocus are optimized for the probe of the Cs-corrected TEM. Each probe parameters are optimized toward minimizing the probe diameter defined as the diameter with 50 percent intensity within. The parameters about other residual aberrations are referred from the parameters of JEOL 2200 TEM in UIUC. The parameters of the optimized probes are shown in Table 2.

	Conventional TEM	Cs-corrected TEM
Aperture	11.7 mrad	22.5 mrad
Spherical aberration	0.52 mm	0.005658 mm
Defocus	-30 nm	-0.247 nm
Two-fold astigmatism	-	1.16 nm
Three-fold astigmatism	-	52.89 nm
Coma	-	122.35 μm

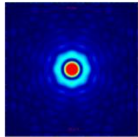
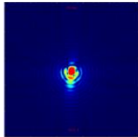



Table2. Optimized parameters of the electron probe in CTEM/Cs-corrected TEM

3.3 CBED/STEM Simulation

Dynamic scattering calculation based on the multislice theory has been carried out using ZMULT code for CBED and STEM simulation. We used the atomic scattering factors calculated by Doyle and Turner²¹ and the absorptive form factors parameterized by Bird and King²³. For STEM simulation, the additional absorptive form factors proposed by Ishizuka¹⁸ was used to describe the thermal diffuse scattering toward the ADF detector. We set up the electrons accelerated to the 200kV and propagated along the zone axis orientation. Since the size of unit cell is inversely proportional to the sampling size of reciprocal space, the large unit cell is needed for CBED and STEM simulation. Thus we incorporate the relaxed structure obtained by the first principle calculation into the large unit cell. For Si 100 direction, we used $20 \times 20 \times 10$ and $20 \times 20 \times 20$ unit cell to simulate CBED or STEM of 5nm thickness and 10nm thickness, respectively. For Si 110 direction, we used $16 \times 12\sqrt{2} \times 6\sqrt{2}$ and $16 \times 12\sqrt{2} \times 14\sqrt{2}$ unit cell to simulate CBED or STEM of 5nm thickness and 10nm thickness, respectively.

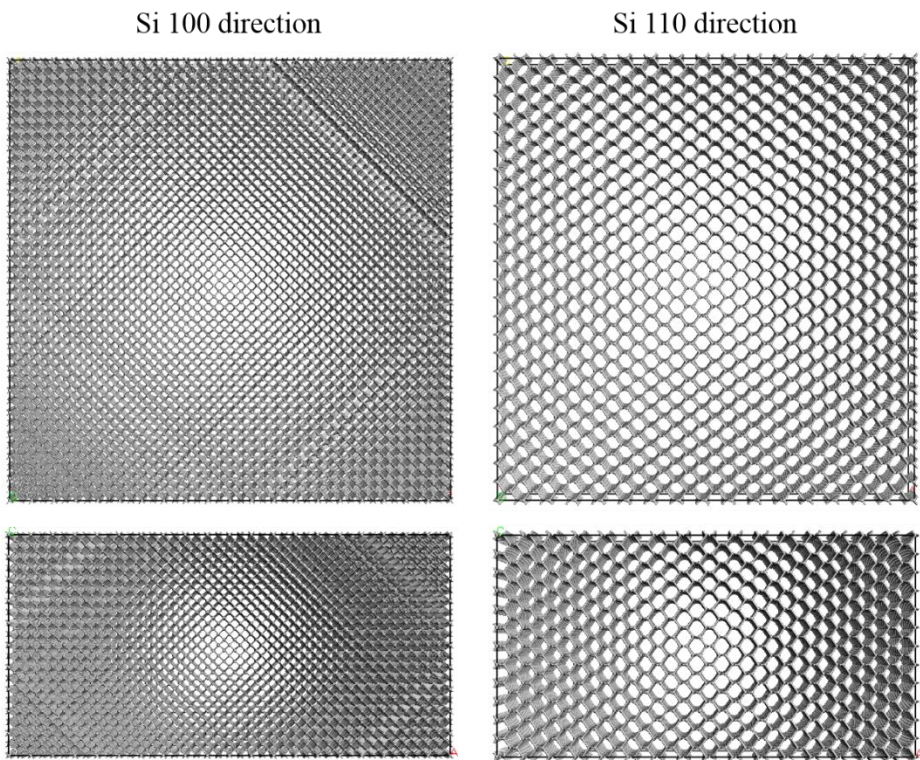


Figure 19. Structure models for CBED/STEM simulation: Si 100, Si 110

4. Results of Calculations

4.1 Silicon 100 Direction

We investigated strain effects of two kinds of point defects: one is a boron dopant atom and the other is a vacancy. Also, we additionally considered a surface roughness to make a division between the strain effect of surface roughness and the strain effect of a point defect. Specifically, Surface roughness indicates the surface reconstruction due to a surface defect. As mentioned above, we simulated the strain field by relaxing the structure with the first principle calculations. Figure 20 is the relaxed structures of three cases. Applying the optimized probes and the relaxed structures, CBED above the defected column were simulated for each case. We additionally simulate CBED of the defectless structure for the reference of scattering angular distribution. We conducted the azimuthal integration of CBED in order to find the specific scattering angular region that distinguishes from the original scattering angular distribution. Figure 21 shows the result of the azimuthal integrations. As a result of simulations, it is expected that the defected column can be distinguishable from other columns if the region between 30mrad and 50mrad is used. Although the strain field due to a boron dopant does not induce a significant modification of scattering angular distribution, the strain field due to a vacancy makes more electrons scatter towards the region between 30mrad and 50mrad and the strain field of surface roughness shows the opposite effects of the vacancy case.

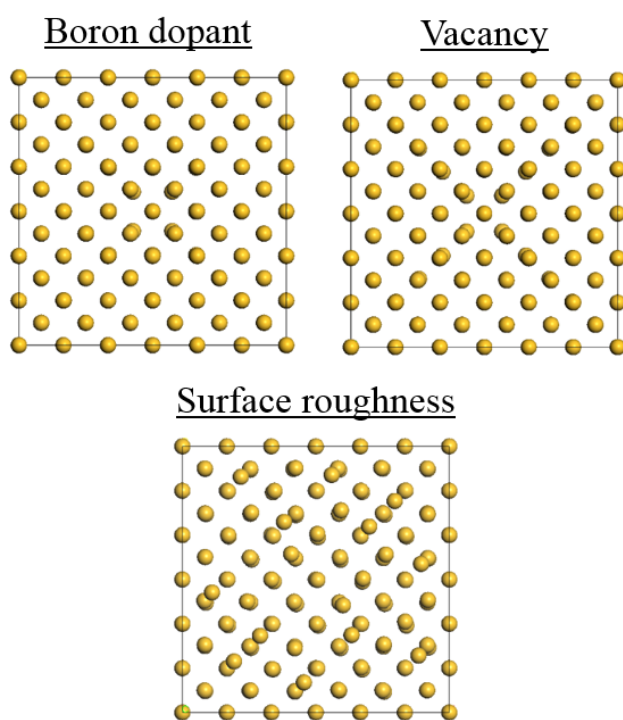
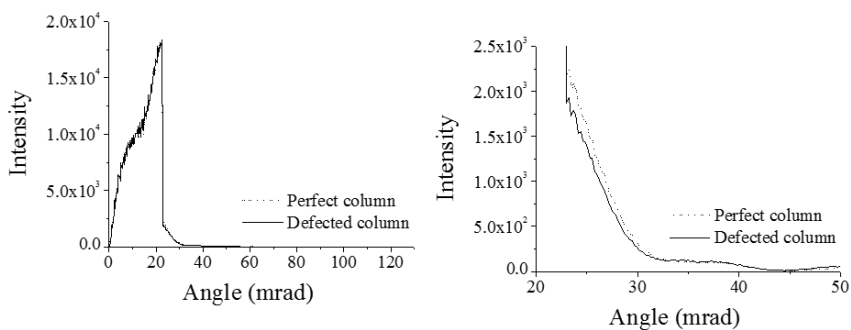
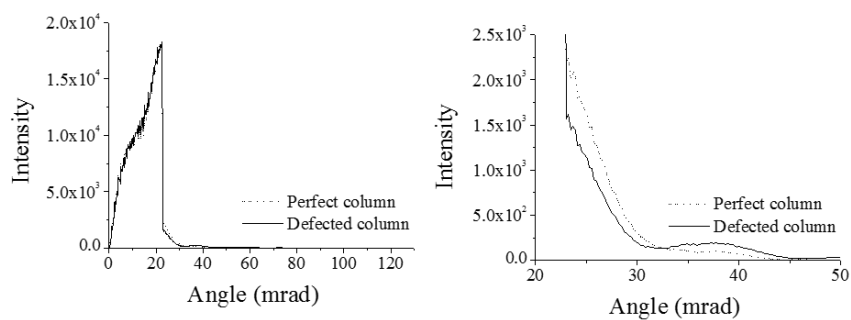


Figure 20. Relaxed structures of boron dopant, vacancy and surface roughness (Si 100 direction)

Boron dopant



Vacancy



Surface roughness

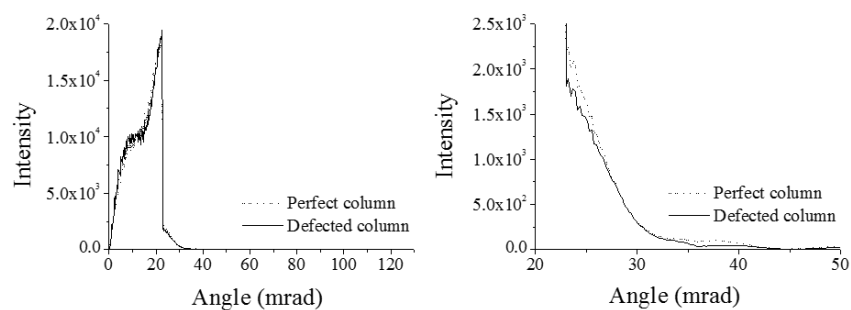


Figure 21. Azimuthal integrations of CBED for a boron dopant case, a vacancy case and surface roughness case (Si100 direction)

As the distinguishable angular distribution between 30mrad and 50mrad was calculated, we conducted STEM image simulations using that detection angle. Figure 22 are the results of STEM simulations. It is noticed that all STEM images show that the intensity of the defected column is about 10% darker than that of other neighboring columns. This indicates that the STEM image is already dominated by thermal diffuse scattering in the 30mrad to 50mrad detection angle. Therefore, we've additionally conducted STEM simulations with only consideration of the elastic scattering. Figure 23 are the results of STEM simulations dealing with only elastic contributions. As expected, the defected columns with a vacancy gave positive contrast comparing to other perfect columns and the defected column by surface reconstruction showed negative contrast. The impressive result of this simulation was the vacancy case with Cs-corrected probe. The defected column is about 200% brighter than other neighboring columns. Therefore, it seems experimentally possible to detect the column with a vacancy if thermal diffuse scattering is suppressed using cold stage holder. It is confirmed that the intensity of elastic contribution is 10 times smaller than that of STEM image considering both elastic and inelastic scattering, which also verify thermal diffuse scattering have already taken dominant portion at the detection angle between 30mrad and 50mrad.

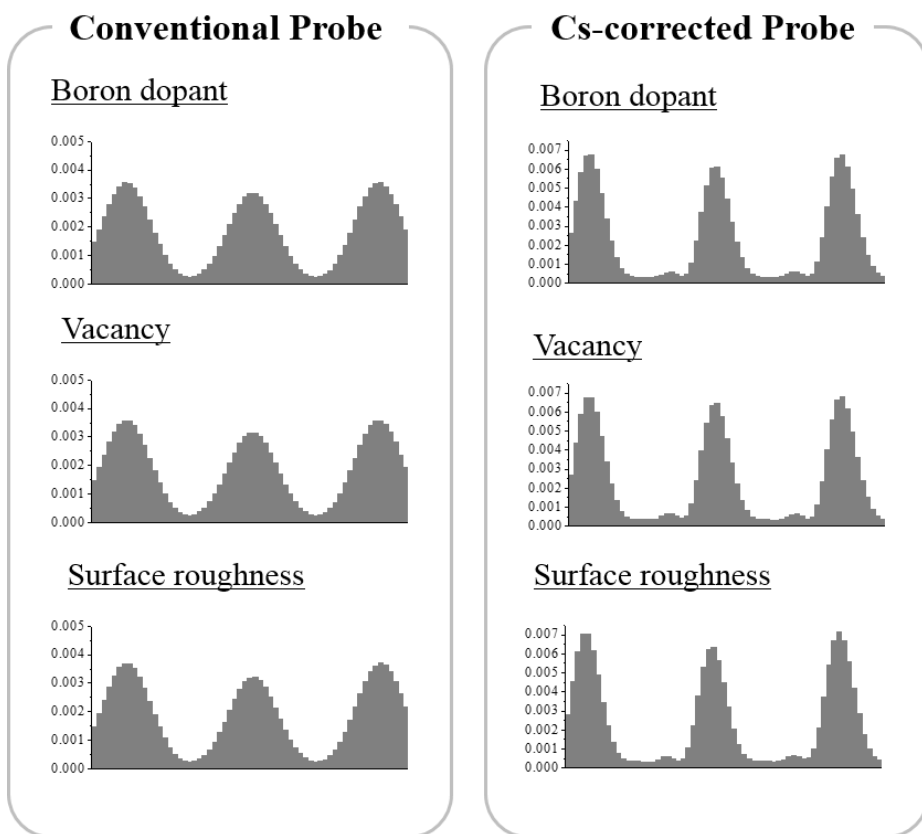


Figure 22. Line scan of simulated STEM images (considering both elastic contribution and inelastic contribution): the center column is the defected column. (Si 100 Direction)

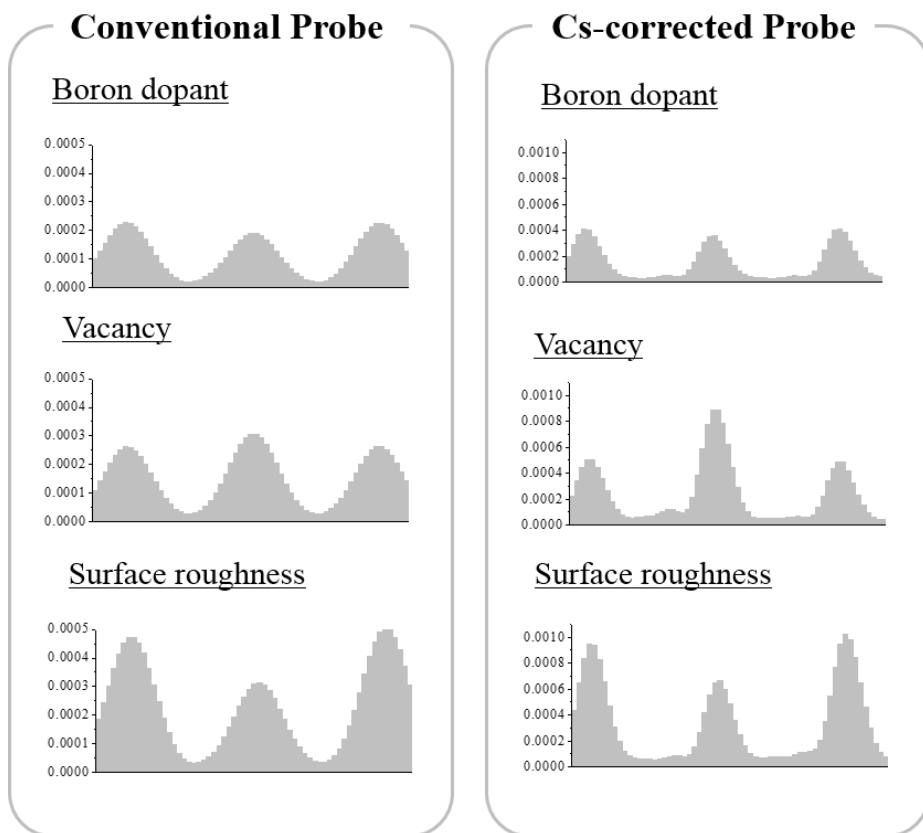


Figure 23. Line scan of simulated STEM images (considering just elastic contribution): the center column is the defected column. (Si 100 Direction)

4.2 Silicon 110 Direction

Silicon 110 direction was also investigated as silicon 100 direction. We

conducted the simulations in the same steps: structural relaxation, CBED simulation and STEM simulation. There was no distinguishable region like 30mrad to 50mrad in the case of silicon 100 direction. Nevertheless, we've tried to carry out STEM simulation with the detection angle between 30mrad and 50mrad. We confirmed that strain effect also exists in silicon 110 direction. However, elastic contribution of STEM image which is directly affected by strain field has the complicated appearance due to asymmetric arrangement of silicon atoms. Therefore, it seems confusing to detect the defected column even though thermal diffuse scatterings are suppressed.

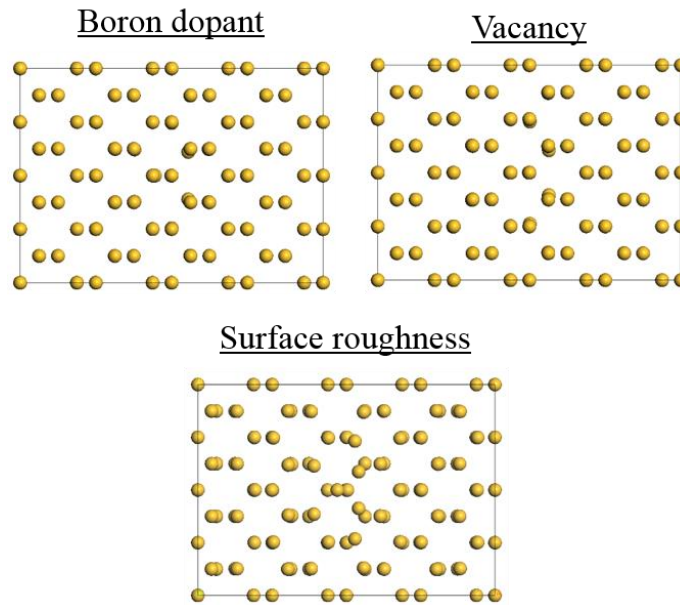


Figure 24. Relaxed structures of boron dopant, vacancy and surface roughness (Si 110 direction)

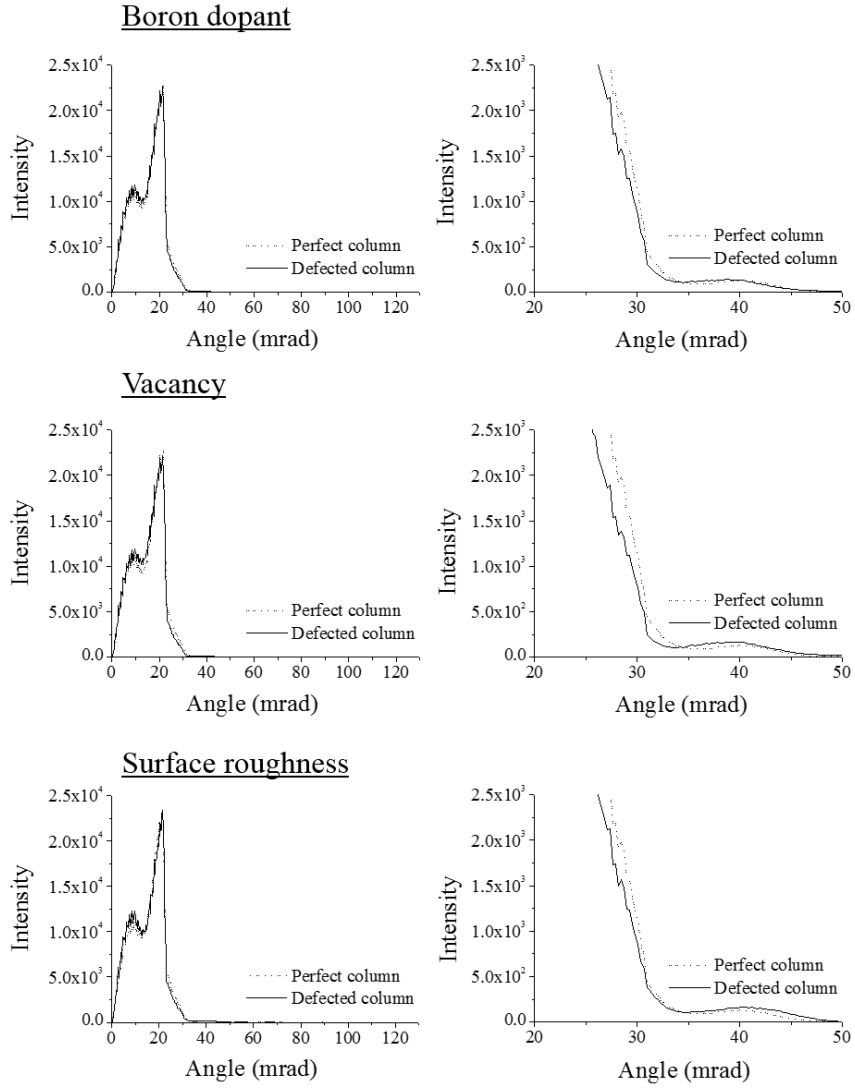


Figure 25. Azimuthal integrations of CBED for a boron dopant case, a vacancy case and surface roughness case (Si110 direction)

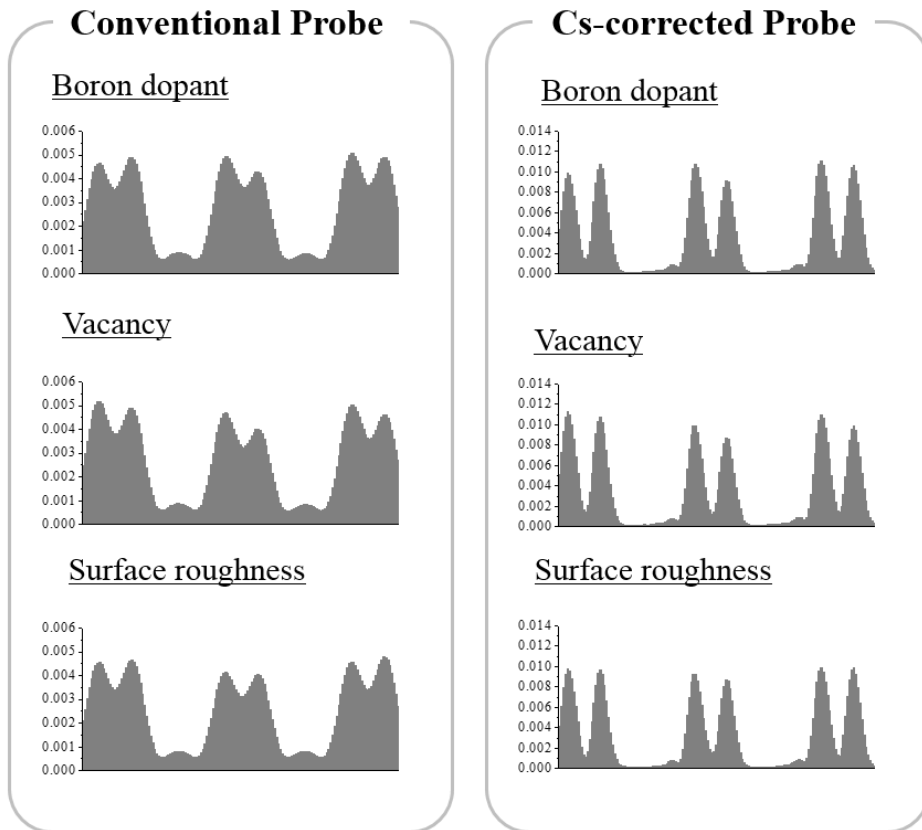


Figure 26. Line scan of simulated STEM images (considering both elastic contribution and inelastic contribution): the right column among center two columns is the defected column. (Si 110 direction)

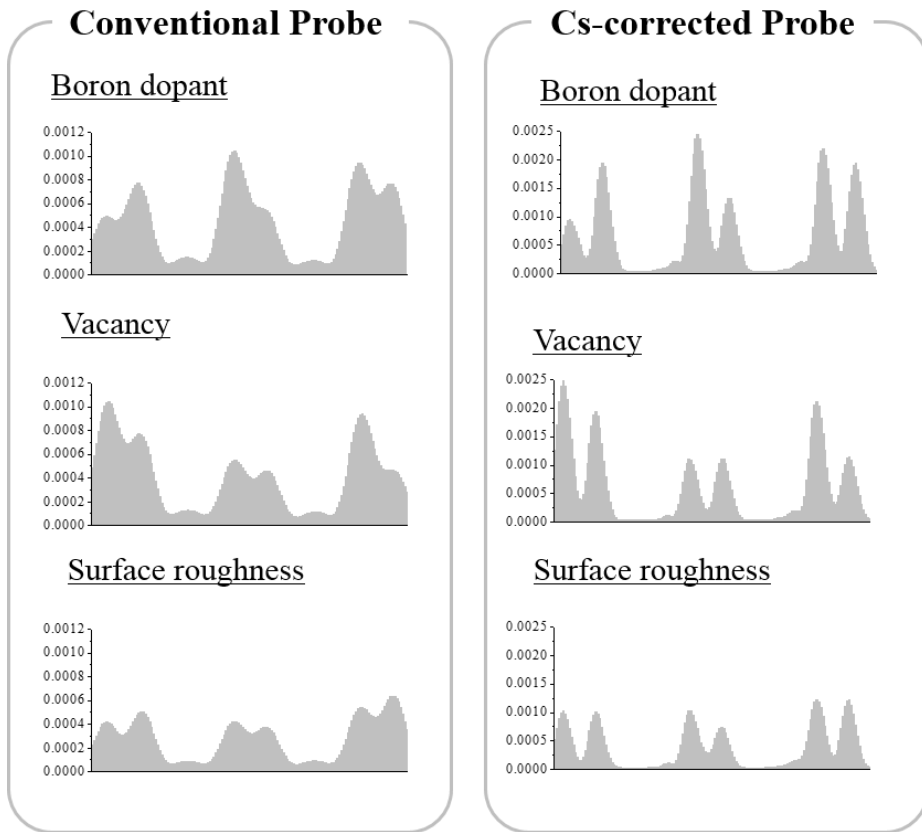


Figure 27. Line scan of simulated STEM images (considering just elastic contribution): the right column among center two columns is the defected column. (Si110 direction)

4.3 Strontium Titanate 100 Direction

Many attempts have been made to detect oxygen vacancy in the transition metal oxide materials, since the physical properties are significantly influenced by the concentration and the dynamics of oxygen vacancies. As many applications of the transition metal oxide such as fuel cell, gas sensor, RRAM or ferroelectric material are on the rise, visualization of oxygen vacancy has been much more required. In this sense, we've investigated oxygen vacancies in strontium titanate. We conducted structural relaxation due to an oxygen vacancy and obtained azimuthal integration through the CBED simulations. Though STEM simulation is not carried out yet, it seems possible to detect an oxygen vacancy in the TiO column if we use the region between 35mrad and 50mrad is used. We will calculate STEM simulations, soon or later.

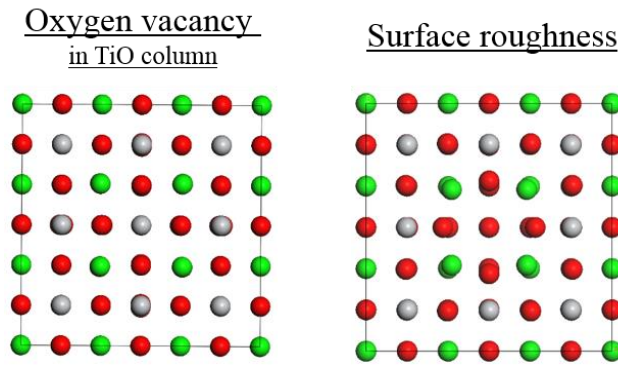
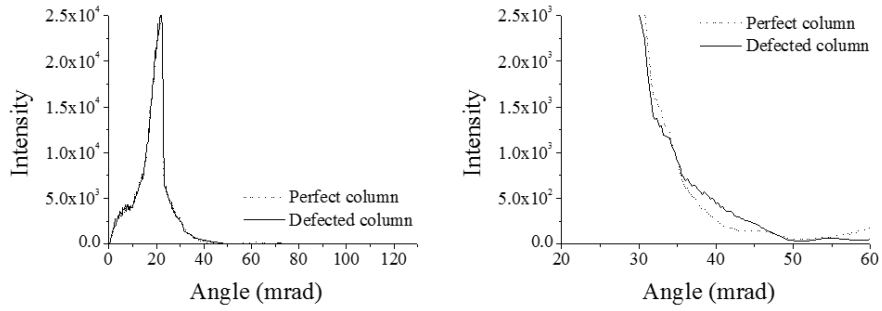


Figure 28. Relaxed structures of oxygen vacancy in TiO column and surface roughness (STO 110 direction)

Oxygen vacancy in TiO column



Surface roughness

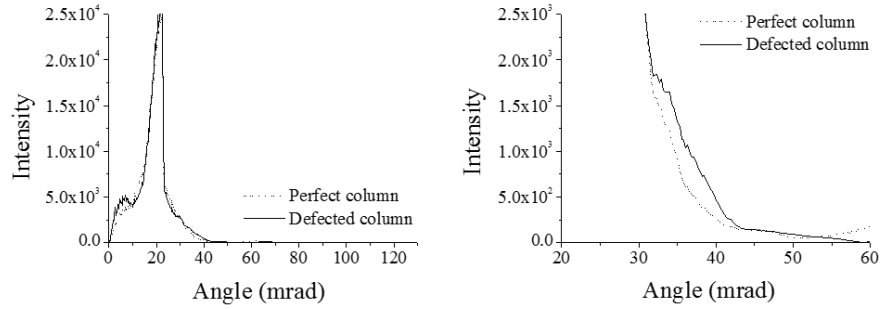


Figure 29. Azimuthal integration of CBED for an oxygen vacancy in TiO column and surface roughness (STO 100)

5. Conclusion

We've studied the feasibility of detecting a light dopant atoms and a vacancy with strain effects through the computer simulation. The strain field is simulated by structural reconstructions with First principle calculations and the propagation of electron waves is simulated with the multislice calculation, one of the dynamic scattering theory. A boron dopant atom, a vacancy in silicon and an oxygen vacancy in strontium titanate have been investigated in our study. We found that the column with a vacancy in silicon would be 200% brighter than other columns if Cs-corrected probe was used and elastically scattered electrons toward 30mrad to 50mrad were utilized. We think the imaging just with elastically scattered electrons is experimentally possible through the cold stage holder which suppress thermal diffuse scatterings. Though we've not carried out the imaging simulation of the strontium titanate case yet, it is expected that detecting an oxygen vacancy in TiO column can be achievable with elastically scattered electrons toward 35mrad to 50mrad. We hope our computer simulation study will give a clue to detect light dopant atoms or a vacancy.

6. References

- 1 John M Cowley, "Diffraction physics," Amsterdam: North-Holland Publication, and New York: Elsevier Publication Co., 1975 **1** (1975).
- 2 Klaus van Benthem, Andrew R Lupini, Mark P Oxley, Scott D Findlay, Leslie J Allen, and Stephen J Pennycook, "Three-dimensional ADF

- imaging of individual atoms by through-focal series scanning transmission electron microscopy," *Ultramicroscopy* **106** (11), 1062-1068 (2006).
- 3 G Behan, EC Cosgriff, Angus I Kirkland, and Peter D Nellist, "Three-dimensional imaging by optical sectioning in the aberration-corrected scanning transmission electron microscope," *Philosophical Transactions of the Royal Society A: Mathematical, Physical and Engineering Sciences* **367** (1903), 3825-3844 (2009).
 - 4 PD Nellist and SJ Pennycook, "Direct imaging of the atomic configuration of ultradispersed catalysts," *Science* **274** (5286), 413-415 (1996).
 - 5 P. M. Voyles, D. A. Muller, J. L. Grazul, P. H. Citrin, and H. J. L. Gossmann, "Atomic-scale imaging of individual dopant atoms and clusters in highly n-type bulk Si," *Nature* **416** (6883), 826-829 (2002).
 - 6 A. R. Lupini and S. J. Pennycook, "Localization in elastic and inelastic scattering," *Ultramicroscopy* **96** (3-4), 313-322 (2003).
 - 7 K. Van Benthem, A. R. Lupini, M. Kim, H. S. Baik, S. Doh, J. H. Lee, M. P. Oxley, S. D. Findlay, L. J. Allen, J. T. Luck, and S. J. Pennycook, "Three-dimensional imaging of individual hafnium atoms inside a semiconductor device," *Applied Physics Letters* **87** (3) (2005).
 - 8 S. H. Oh, K. Van Benthem, S. I. Molina, A. Y. Borisevich, W. Luo, P. Werner, N. D. Zakharov, D. Kumar, S. T. Pantelides, and S. J. Pennycook, "Point defect configurations of supersaturated Au atoms inside Si nanowires," *Nano Letters* **8** (4), 1016-1019 (2008).
 - 9 Z. Yu, D. A. Muller, and J. Silcox, "Study of strain fields at a-Si/c-Si interface," *Journal of Applied Physics* **95** (7), 3362-3371 (2004).
 - 10 John M Cowley and A F Moodie, "The scattering of electrons by atoms and crystals. I. A new theoretical approach," *Acta Crystallographica* **10** (10), 609-619 (1957).
 - 11 K. Ishizuka and N. Uyeda, "A new theoretical and practical approach

- to the multislice method," *Acta Crystallographica Section A* **33** (5), 740-749 (1977).
- 12 D Van Dyck, "The path integral formalism as a new description for the diffraction of high-energy electrons in crystals," *physica status solidi (b)* **72** (1), 321-336 (1975).
 - 13 J. M. Cowley, "Applications of electron nanodiffraction," *Micron* **35** (5), 345-360 (2004).
 - 14 W Kossel and G Möllenstedt, "Electron interference in a convergent beam," *Nature* **26**, 660 (1938).
 - 15 Peter D Nellist, "The principles of STEM imaging", in *Scanning Transmission Electron Microscopy* (Springer, 2011), pp. 91-115.
 - 16 ZL Wang and JM Cowley, "Simulating high-angle annular dark-field STEM images including inelastic thermal diffuse scattering," *Ultramicroscopy* **31** (4), 437-453 (1989).
 - 17 R. F. Loane, P. Xu, and J. Silcox, "Thermal vibrations in convergent-beam electron diffraction," *Acta Crystallographica Section A* **47** (3), 267-278 (1991).
 - 18 K. Ishizuka, "A practical approach for STEM image simulation based on the FFT multislice method," *Ultramicroscopy* **90** (2-3), 71-83 (2002).
 - 19 Earl J Kirkland, *Advanced computing in electron microscopy*. (Springer, 2010).
 - 20 S. J. Pennycook and D. E. Jesson, "High-resolution Z-contrast imaging of crystals," *Ultramicroscopy* **37** (1-4), 14-38 (1991).
 - 21 P. A. Doyle and P. S. Turner, "Relativistic Hartree-Fock X-ray and electron scattering factors," *Acta Crystallographica Section A* **24** (3), 390-397 (1968).
 - 22 CR Hall and PB Hirsch, "Effect of thermal diffuse scattering on propagation of high energy electrons through crystals," *Proceedings of the Royal Society of London. Series A. Mathematical and Physical*

- Sciences **286** (1405), 158-177 (1965).
- 23 D. M. Bird and Q. A. King, "Absorptive form factors for high-energy electron diffraction," *Acta Crystallographica Section A* **46** (3), 202-208 (1990).
- 24 L. M. Peng, G. Ren, S. L. Dudarev, and M. J. Whelan, "Robust parameterization of elastic and absorptive electron atomic scattering factors," *Acta Crystallographica Section A: Foundations of Crystallography* **52** (2), 257-276 (1996).
- 25 G. Kresse and J. Furthmüller, "Efficient iterative schemes for ab initio total-energy calculations using a plane-wave basis set," *Physical Review B - Condensed Matter and Materials Physics* **54** (16), 11169-11186 (1996).

한글 초록

2000년대 초반 주사투과전자현미경(STEM)의 sub angstrom 분해능이 구면수차보정 전자기렌즈의 도입으로 가능해진 이후, single atomic imaging 혹은 light element imaging과 같은 STEM의 측정한계를 뛰어 넘으려는 시도가 전자현미경 학계에서 많이 있었다. 2000년대 중반 HADDF-STEM을 이용해 무거운 원소의 단일원자를 관측하는데 성공하였고, 2010년에 들어서는 ABF-STEM을 이용한 가벼운 원소 기둥 관측을 연달아 성공하였다. 하지만 아직도 가벼운 불순물 원자 혹은 정공의 관측은 불가능한 것으로 알려져 있다. 우리는 기존 방법의 틀에서 벗어나 점 결함을 strain effect를 이용하여 측정하면 가벼운 불순물 원소와 정공을 구분할 수 있지 않을까 기대하고 있다. 물론 점 결함 하나가 만들어내는 strain field가 산란의 전체적인 양상을 바꾸지는 못하겠지만 특정 각도에서는 다른 양상으로 산란이 일어날 수 있다. 만약 우리가 다른 산란 정보를 주는 각도를 예측하고 그 각도로 산란되는 전자만을 이용하여 imaging한다면, 가벼운 불순물 원자 및 정공을 시각화하는 것이 가능하다 생각하고 있다.

본 연구에서는 strain effect를 이용한 가벼운 불순물 원자와 정공을 관측의 구현 가능성을 컴퓨터 전산모사를 통해 연구하였다. 점 결함이 만들어내는 Strain field는 제1원리 계산의 일종인 범 밀도 함수 이론을 이용하여 구현하였고, 물질 내 전자의 산란은 dynamic 산란 이론의 일종인 multislice 방법을 이용하여 계산하였다. 계산 결과, 비탄성 산란(열 확산 산란)을 억제시키고 strain effect가 많이 일어나는 산란각도만을 이용한다면 가벼운 불순물 원소 및 정공을

시각화하는 것이 가능할 것으로 예측하였다. 구체적으로, 30mrad에서 50mrad 사이의 각도로 탄성산란 된 전자들만을 이용해 규소 결정에 들어있는 정공을 imaging한다면, 정공을 가진 기둥이 다른 일반적인 기둥들보다 두 배 가량 밝은 contrast를 보임을 계산을 통해 확인하였으며, STO 내의 정공 역시 35mrad에서 50mrad 산란각도를 이용하면 정공을 시각화할 수 있을 것으로 예상하고 있다. 물론 실험을 통해 본 방법을 구현하기 위해서는 아직 CCD의 성능이 필요할 것으로 생각되지만, 본 연구의 방법으로 가벼운 불순물 원소 혹은 정공을 시각화하는 데 성공한다면 그 자체 만으로도 전자현미경 분야에서 의미 있을 뿐만 아니라 인접한 다른 재료 과학분야에도 큰 기여를 할 수 있을 것으로 기대하고 있다.

주요어: 점 결함 시각화, 전자현미경, 수렴각 전자회절, 주사투과전자현미경, strain contrast, 전자 산란, dynamic 산란 이론

학번: 2012-20616